Journal of Computational Physics 229 (2010) 73–106

Contents lists available at ScienceDirect

Journal of Computational Physics

journal homepage: www.elsevier.com/locate/jcp

Eulerian–Lagrangian multiscale methods for solving scalar equations – Application to incompressible two-phase flows

Stéphane Vincent [a,*], Guillaume Balmigère [b], Jean-Paul Caltagirone [a], Erick Meillot [b]

[a] Universite Bordeaux 1, Transferts, Ecoulements, Fluide, Energétique (TREFLE), UMR 8508, ENSCPB, 16 Avenue Pey-Berland, 33607 PESSAC Cedex, France
[b] Commissariat à l'Energie Atomique (CEA) Le Ripault, BP 16, 37000 Monts, France

ARTICLE INFO

Article history:
Received 11 September 2008
Received in revised form 30 April 2009
Accepted 8 September 2009
Available online 23 October 2009

Keywords:
Interface tracking
Transport equation
Volume Of Fluid (VOF)
Eulerian–Lagrangian method

ABSTRACT

The present article proposes a new hybrid Eulerian–Lagrangian numerical method, based on a volume particle meshing of the Eulerian grid, for solving transport equations. The approach, called Volume Of Fluid Sub-Mesh method (VOF-SM), has the advantage of being able to deal with interface tracking as well as advection–diffusion transport equations of scalar quantities. The Eulerian evolutions of a scalar field could be obtained on any orthogonal curvilinear grid thanks to the Lagrangian advection and a redistribution of particles on the Eulerian grid. The Eulerian concentrations result from the projection of the volume and scalar informations handled by the particles. The particle velocities are interpolated from the Eulerian velocity field. The VOF-SM method is validated on several scalar interface tracking and transport problems and is compared to existing schemes within the literature. It is finally coupled to a Navier–Stokes solver and applied to the simulation of two free-surface flows, i.e. the two-dimensional buckling of a viscous jet during the filling of a square mold and the three-dimensional dam-break flow in a tank.

1. Introduction

The numerical simulation of scalar advection or transport on fixed structured grids is of major importance in most multiphase flows, combustion or plasma problems, as well as in environmental research. During the last two decades, many research efforts have been devoted to tracking interfaces between immiscible fluids on the one hand and, on the other hand, to transporting specie concentrations or temperatures in incompressible flows. If we assume that the flow field is solved independently thus providing the velocity field **u**, all the previous problems involve the resolution of a scalar transport equation on a variable ϕ.

$$\alpha\left(\frac{\partial\phi}{\partial t}+\mathbf{u}\cdot\nabla\phi\right)=\nabla\cdot(D\nabla\phi) \tag{1}$$

According to the type of physics related to Eq. (1), the coefficients α and D are defined in different ways: $\alpha=1$ and $D=0$ when considering an interface tracking [43] or an air quality model [36]; $\alpha=\rho C_p$, where ρ is the density and C_p the specific heat, and D is the conductivity if the temperature convection and diffusion are of interest [40]; $\alpha=1$ and D is a diffusion coefficient if the transport of a specie concentration is modeled [29].

Whatever the sense of Eq. (1), two types of numerical approaches are proposed depending on whether ϕ is related to an interface tracking or to the advection or transport of a diffusive scalar quantity. In the first class of problems, ϕ represents the

* Corresponding author. Tel.: +33 (0) 5 56 84 27 07; fax: +33 (0) 5 56 84 66 68.
E-mail address: vincent@enscpb.fr (S. Vincent).

0021-9991/$ - see front matter © 2009 Elsevier Inc. All rights reserved.
doi:10.1016/j.jcp.2009.09.007

local volume fraction of one fluid in each grid cell used to build the two-phase flow characteristics at each time step. For example, the density and dynamic viscosity are defined as follows:

$$\begin{aligned}\rho &= \rho_1\phi + \rho_0(1-\phi)\\ \mu &= \frac{\mu_0\mu_1}{\mu_0\phi + \mu_1(1-\phi)}\end{aligned} \tag{2}$$

Eq. (2) ensures the coupling between the interface evolution and the flow solving. Among the most popular numerical methods for simulating the advection of ϕ can be cited the level-set approach [14], which consists in using a distance function for simulating the evolution of ϕ, the Volume Of Fluid (VOF) method [19,1], which is based on the reconstruction of the interface in all grid cells, the front-tracking technique [47], which advects markers located on the interface to build ϕ at each time step, or the Marker And Cell (MAC) algorithm [41], which uses the advection of markers distributed into each grid cell to obtain ϕ after a local integration of the volume fraction held by the markers. All these methods have been extensively improved and combined [2] in order to upgrade their performance and accuracy in terms of spatial convergence and consistency with respect to mass conservation. They have been evaluated and tested on scalar problems, for example by Rider and Kothe [42].

Concerning the numerical simulation of the second class of problems, i.e. diffuse scalar transport, the most natural approach consists in discretizing Eq. (1) with numerical schemes initially designed for hyperbolic scalar equations such as TVD [28] or WENO [22] schemes. However, it has been demonstrated that these schemes involve numerical diffusion and tend to smooth the sharp maxima and minima of the solution. Thus, an accurate description of scalar quantities cannot be ensured when ϕ is advected in a velocity field involving strong shearing [49,42,12]. Many other numerical methods have been designed to solve Eq. (1) such as the GLK fourth-order Taylor–Galerkin algorithm, the ASD approach based on Taylor expansion with Fourier derivatives, the QSTSE approach that uses fourth-order Taylor expansion with quintic splines or the Bott scheme that belongs to the class of non linear flux normalization schemes. A review and comparison of all these numerical schemes is proposed by Nguyen and Dabdub [36]. As for hyperbolic discretization schemes, each method has its merits but generates spurious numerical effects such as artificial diffusion or flotsam when the scalar profile is sharp or when shearing flows are considered.

The present paper presents the development and validation of a unified numerical method for both interface tracking problems and diffuse scalar transport. This method aims at managing, in three dimensions, the macroscopic evolutions of the scalar quantity ϕ on a structured Eulerian curvilinear grid thanks to a Lagrangian description of the scalar advection of ϕ. This is done by generalizing the spirit of MAC techniques [41], Particle In Cell (PIC) methods [8] and Moving Particle Semi-implicit (MPS) approaches [32]. The objectives have been to manage any profile of ϕ while ensuring spatial convergence order, accuracy and mass conservation with quality levels at least comparable to the best Eulerian methods and schemes found in the literature.

The article is organized as follows: Section 2 presents a new numerical approach, called the Volume Of Fluid Sub-Mesh (VOF-SM) method, based on a Lagrangian description of scalar quantities for solving Eulerian scalar evolutions. This method uses the distribution and advection of particles at a scale smaller than the macroscopic Eulerian grid scale. The macroscopic scalar quantities are then constructed from a projection of the Lagrangian scalar description to the fixed grid. In Section 3, the VOF-SM method is dedicated to treating interface tracking problems based on analytical velocity fields. The application of the VOF-SM approach to scalar transport test cases involving analytical velocity fields is presented in Section 4. Sections 3 and 4 aim at providing a detailed analysis of the performances of the VOF-SM method. Accuracy and convergence orders are estimated and results are compared to reference simulations of the literature. The simulation of jet buckling in a 2D cavity and the 3D dam-break flow are presented in Section 5 in order to illustrate the ability of the VOF-SM method to deal with free-surface flows where complex interface rupture and coalescence occur. Finally, the benefits of the method is summarized and perspectives for future applications and developments of the VOF-SM method are discussed.

2. A mixed Eulerian–Lagrangian method for solving scalar equations

The aim of the present study was to design a general numerical approach for solving scalar transport equations. Such a method must be able to deal with interface tracking on orthogonal curvilinear grids in order to be applicable to industrial flows in complex geometries while maintaining a high convergence order when strong interface stretching or tearing are involved. Moreover, the same numerical method is used to tackle the advection of sharp or smooth continuous scalar profiles with equivalent qualities. In addition, the method must be applicable in three dimensions.

As discussed in the previous sections, all the existing numerical methods that are based on Eulerian approaches, i.e. VOF methods, level-set techniques, TVD and WENO schemes or front-tracking approaches, suffer from numerical artefacts or are only applicable to specific scalar advection problems. Based on existing reports on mixed Lagrangian/Eulerian discretizations [4] and modeling of transport phenomena, we propose to build a numerical method that solves the general form of the scalar transport Eq. (1) in a Eulerian representation, similarly to Volume Of Fluid techniques from a Eulerian point of view, thanks to a Lagrangian discretization. The objective of such a method is to provide a sub-mesh description of thin interface or concentration structures at scales smaller than the Eulerian grid size. The method is called Volume Of Fluid Sub-Mesh method (VOF-SM).

2.1. Existing methods

Several recent studies have been devoted to mixed Eulerian–Lagrangian numerical methods designed for solving Eulerian interface tracking. Among them, the Eulerian–Lagrangian Marker and Micro Cell (ELMMC) method of Radd and Bidoae [41] consists in tracking the interface between two fluids by massless unconnected markers located at the interface. A fixed Cartesian grid is used to discretize the motion equations. In this approach, the velocity field is solved in only one phase. The empty surface and full grid cells are flagged thanks to the markers' positions. The surface cells are subdivided into micro cells in order to prescribe free-surface boundary conditions. The method is not analyzed nor discussed for scalar advection test cases concerning mass conservation and space convergence order. Its physical consistency is demonstrated through the comparison between a 3D dam-break flow and experiments. A rather good agreement is found between simulations and measurements on the time evolution of local velocities at various locations. The convergence of ELMMC is studied on the water flow over a spillway geometry. Droplet interaction and coalescence as well as cavity filling problems are also presented.

Another approach is the hybrid particle-mesh method of Liu et al. [32], which is dedicated to the two-dimensional simulation of incompressible two-phase flows. A set of particles is distributed in one phase as in a standard meshless MPS method in order to track interfaces and the conservation equations are solved on a fixed Cartesian grid. The markers are massless. The mass conservation is ensured by a projection method and particle velocity corrections. The Eulerian interfacial quantities are obtained by projecting the particle characteristics on the Eulerian grid thanks to kernel functions. The method is not validated on standard advection or interface tracking problems. No detailed convergence study is provided on the interface tracking. The mixed Eulerian–Lagrangian method is validated on droplet flows driven by capillary forces. A second-order convergence in space is observed on the Laplace law.

The hybrid particle/grid method of Ishii et al. [21] combines the use of the Constrained Interpolation Profile CIP approach, for solving the three-dimensional Eulerian evolutions of two-phase flows with the MPS method, for describing small interfacial structures whose space scale is smaller than the local Eulerian mesh size. This MPS/CIP approach considers massless markers and unstructured grids. The velocities given by the Lagrangian interface description and those provided by the Eulerian CIP technique are combined in the mixed cells cut by the interface thanks to linear phase average formulas. No convergence analysis nor convergence study is provided on standard advection test cases. The MPS/CIP method is validated on the collapse of a water column through a comparison of simulation results and experimental measurements. The qualitative comparison with the results of Martin and Moyce [35] shows a correct general behavior whereas a gap of 10–20% exists between the simulation and the measurements concerning the time evolution of the leading edge of the water column. Moreover, the MPS/CIP simulations are similar to those obtained by Hirt and Nichols [19]. However, their VOF method is not up to date and comparisons to more recent and accurate VOF methods would be interesting. Finally, the MPS/CIP method is applied to the simulation of the behavior of a liquid film in a fuel injector.

To sum up the existing approaches, the recent works of Bierbrauer and Zhu [4] are dedicated to modeling two-dimensional multiphase flows by combining Eulerian Godunov discretizations to Marker Particle Projection Schemes (GMPPS). A Lagrangian method, based on massless particles, is designed to track a fluid color function with a high convergence order. A one-fluid formulation of motion equation is used to model multiphase flows. The GMPPS method is accurately evaluated on benchmark tests involving analytical velocity fields verifying divergence free conditions. It is demonstrated that the mass conservation is ensured with a percentage error lower than 1–2%. Moreover, second-order accuracy is measured for all the simulations.

2.2. The Volume Of Fluid Sub-Mesh (VOF-SM) method

All the methods presented in the previous section are able to solve 2D or 3D multiphase flows and couple the volume or surface marker description of the interfacial evolution to Eulerian discretizations of the motion equations. However, these techniques can only describe the Eulerian evolution of a binary volume fraction, solution of Eq. (1) with $D = 0$. Similarly, the method presented herein is based on the principle that only a Lagrangian approach can deal with an accurate and non-diffusive Eulerian description of ϕ solution of (1), for which the scales are smaller than the Eulerian space step. The aim is to generalize the coupling between particle and Eulerian approaches to all types of scalar equations, to design a general method applicable to curvilinear structured grids, to explain the management of particles and their possible redistribution if required in the case of shearing flows for example and to provide a detailed analysis of space convergence and mass conservation on standard scalar advection tests.

2.2.1. Initialization of the markers

The computational domain Ω is discretized according to a three dimensional Eulerian curvilinear staggered grid. The scalar fields (pressure, temperature, color function, species concentration) are resolved on the scalar grid made up of computational cells centered at the position $(xi_{i,j,k}, yi_{i,j,k}, zi_{i,j,k}), (i,j,k) \in \Omega$. The velocity, on the other hand, field is discretized on a secondary staggered grid. The computational domain is initially seeded with markers, the number of which is equal in each computational cell. The markers are regularly spaced inside the cell as illustrated in Fig. 1 for a two-dimensional Cartesian grid with four particles per cell (ppc). Each marker m is assigned the number of its reference cell K_m, its initial volume δV_m, its local position in the cell $K_m = (x_m, y_m, z_m)$ and a phase data ϕ_m^p, which is a function of the initial phase

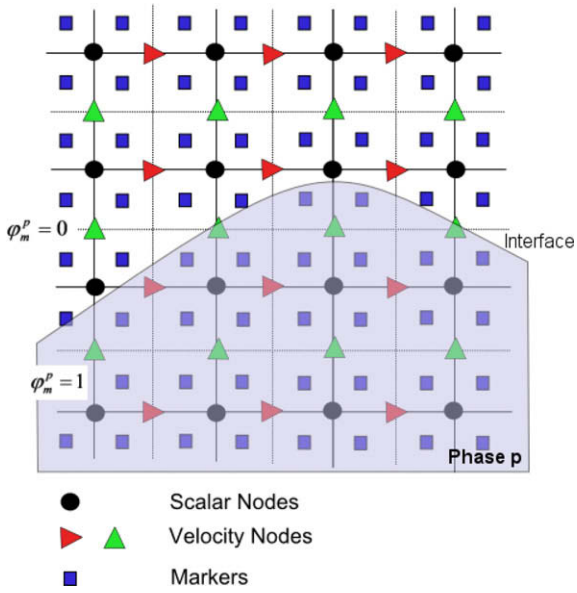

Fig. 1. A two-dimensional staggered Cartesian grid and marker distribution (4 ppc).

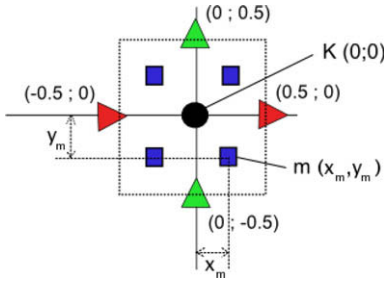

Fig. 2. A local coordinate system of a grid cell centered on the scalar node K.

distribution. It is stated that $\phi_m^p = 1$ if m is in the phase p and that $\phi_m^p = 0$ otherwise. If n particles are distributed $V_K$in each space directions and in each computational cell, we define $\delta V_m = \frac{V_{Km}}{n^3}$ in three dimensions, where V_{Km} is the volume of the Eulerian cell K_m.

For the sake of convenience in the particle management and transport, the grid $(i,j,k) \in \Omega$ defined in the physical coordinate system is transformed into a unitary regular one (see Fig. 2). Thus, the markers have local coordinates ranging from -0.5 to 0.5 in the three directions, independently of the local grid size and shape. As a result, the Eulerian velocity field in the local coordinate system is modified as follows:

$$v^t_{i+1/2,j,k} = \frac{v_{i+1/2,j,k}}{\Delta x_{i+1/2,j,k}} \tag{3}$$

$$v^t_{i+1/2,k} = \frac{v_{i,j+1/2,k}}{\Delta y_{i,j+1/2,k}} \tag{4}$$

$$v^t_{i,j,k+1/2} = \frac{v_{i,j,k+1/2}}{\Delta z_{i,j,k+1/2}} \tag{5}$$

where index t is associated to the transformed coordinate system and $\Delta x_{i+1/2,j,k}$, $\Delta y_{i,j+1/2,k}$ and $\Delta z_{i,j,k+1/2}$ are the local metrics of the curvilinear Eulerian grid in each space direction. On a staggered Cartesian grid, $v^t_{i+1/2,j,k}$, $v^t_{i,j+1/2,k}$ and $v^t_{i,j,k+1/2}$ correspond to velocity components in the x-, y- and z-directions respectively.

2.2.2. Transport of the markers

2.2.2.1. Management of time. At each time step, the markers are advected over a full time step δt. The physical time step is split into sub-steps $8t\prime$, according to a specific Courant–Friedrichs–Levy CFL-like condition defined as:

$$\delta t' = \frac{0.5}{|\mathbf{v}^t_{max}| \cdot n} \tag{6}$$

where $|\mathbf{v}^t_{max}|$ is the maximum value of the velocity norm in the transformed coordinate system, and n is the initial number of particles per cell in each direction. This CFL condition ensures that the advection sub-step will not transport the particles beyond the volume δV_m that they are supposed to occupy.

2.2.2.2. Velocity interpolation. For each marker, the substep involves the resolution of the relation $\frac{d\mathbf{x}^t}{dt} = \mathbf{v}^t$, which is realized through a time splitting procedure. The velocity field is either provided by an analytical function or calculated as part of the resolution algorithm. Thus, we benefit from the discrete knowledge of the velocity on the staggered grid, which must be interpolated to the marker position. This procedure is achieved for each velocity component through a Q1 interpolation procedure from the eight velocity nodes surrounding the markers in three dimensions. The interpolation coefficients are easily known since the velocity nodes are located at coordinates –0.5, 0 or 0.5 in the local transformed coordinate system for any cell in the computational domain. Therefore, the only variables required for the interpolation subroutine are the surrounding velocities and the relative position vector $\mathbf{d}_m = (d_m, I, d_m, J, dm, K)$ of the marker to one of its surrounding velocity nodes I, J, K. Assuming this node is the front bottom left corner of the box defined by the eight velocity nodes surrounding the marker, the cell to particle interpolation of one component v^t of the local velocity field $\mathbf{v}^t$, in the transformed coordinate system, is given by the expression:

$$\begin{aligned} v^t_m = &\left[(l - d_{m,I})(1 - d_{m,J}) \cdot v^t_{I,J,K} + d_{m,I}(1 - dm,J) \cdot v^t_{I+1,J,K} + d_{m,I}d_{m,J} \cdot v^t_{I+1,J+1,k} + (1 - d_{m,I})d_{m,J} \cdot v^t_{I+1,J+1,k}\right] \cdot (1 - d_{m,K}) \\ &+ \left[(1 - d_{m,I})(1 - d_{m,J}) \cdot v^t_{I,J,K+1} + d_{m,I}(1 - d_{m,J}) \cdot v^t_{I+1,J,K+1} + d_{m,I}d_{m,J} \cdot v^t_{I+1,J+1,k+1} + (1 - d_{m,I})d_{m,J}\right] \cdot v^t_{I+1,J+1,K+1} \cdot d_{m,k} \end{aligned}$$

2.2.2.3. Transport. At first, the velocity is interpolated at the initial position $\mathbf{x}^0_m$ of the marker, which is advected by the interpolated velocity $\mathbf{v}^{t,0}_m$ over $\frac{\delta t'}{2}$. It provides an intermediate position defined by:

$$\mathbf{x}'_m = \mathbf{x}^0_m + \frac{\delta t'}{2}\mathbf{v}^{t,0}_m \tag{7}$$

The transformed velocity field is interpolated at the intermediate position $\mathbf{x}'_m$. This provides an intermediate value $\mathbf{v}'_m t$ of the particle velocity, which will be used to bring the particle to its final position $\mathbf{x}^f_m$ in the internal sub-step:

$$\mathbf{x}^f_m = \mathbf{x}^0_m + \delta t' \frac{\left(\mathbf{v}^{t,0}_m + \mathbf{v}'^t_m\right)}{2} \tag{8}$$

2.2.2.4. Boundary conditions. During its travel along a time sub-step, a marker may cross a boundary of the computational domain. Various treatments are obviously required, depending on whether the boundary is open, periodic or solid.

In the case of a periodic boundary condition, the particle exits the computational domain and its new reference node is located at the opposite side. Its positions in the transformed coordinate system centered on the local node K_m are given by the amount the marker exceeds the periodic boundary. The solid boundary condition type is accounted for by a reflection of the calculated position into the domain. The markers exceeding open boundaries are given a characteristic phase data value $\phi_m = 10 \gg 1$ which renders it possible to treat them differently in the particle to Eulerian mesh projection, i.e. the computing of the color function, and the redistribution of the particle.

2.2.2.5. Updating the marker data. Each marker is characterized by its reference node m, its volume V_m, its local position in the reference node cell centered coordinate system and its phase data ϕ_m. Along a time sub-step, a marker may move from its reference cell to a neighboring cell. This data is easily updated since the new reference cell is necessarily a neighboring cell due to the current condition. Moreover, in the local transformed coordinate system, the determination of the reference cell and the computation of the new maker local position is straightforward.

The interpolation, transport, boundary condition management and marker data algorithms are general and can be applied to any orthogonal curvilinear grid, according to the algorithm presented in Fig. 3.

2.2.3. Particle to Eulerian mesh projection

Once the numerical characteristics of the markers are updated, at the end of the transport step, the phase information ϕ_m is projected to the scalar Eulerian grid cells $(i, j, k) \in \Omega$ so as to reconstruct the macroscopic color[1] function $C_{i,j,k}$. Initially, each computational cell contains the same number of particles, wherefore each particle transports a fixed amount δV_m of fluid along the simulation. Assuming δV_m has a parallelepiped shape in the transformed coordinate system, the particle-mesh projection can be carried out analytically, in a geometrical manner as illustrated in Fig. 4, as:

[1] For interpretation of color in Figs. 4, 9 and 15, the reader is referred to the web version of this article.

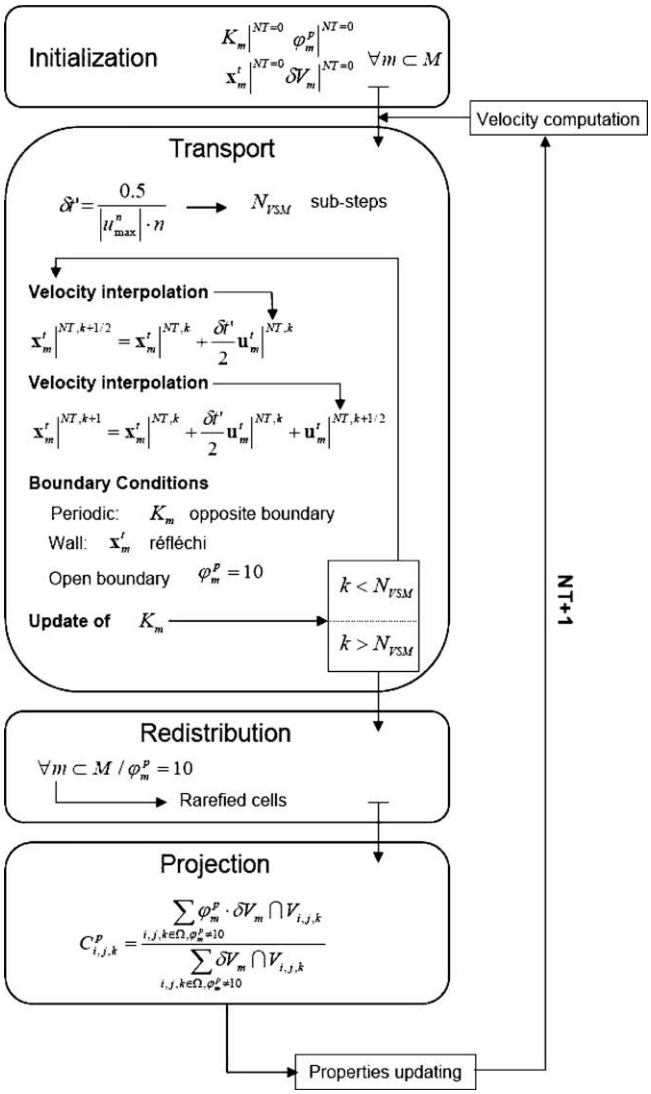

Fig. 3. General algorithm of the VOF-SM method.

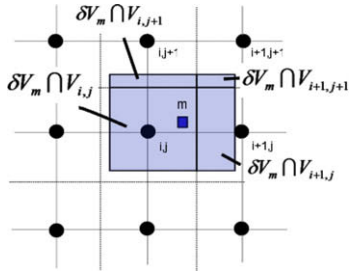

Fig. 4. Particle to Eulerian grid projection method in two dimensions.

$$C_{i,j,k}^p = \frac{\sum_{\mathbf{x}_m \in \Omega_{i,j,k}, \phi_m^p \neq 10} \phi_m^p \cdot \delta V_m \cap V_{i,j,k}}{\sum_{\mathbf{x}_m \in \Omega_{i,j,k}, \phi_m^p \neq 10} \delta V_m \cap V_{i,j,k}} \tag{9}$$

Here Vi,j,k is the volume of the cell (i,j,k) and $\delta V_m \cap V_{i,j,k}$ is its intersection with the volume of fluid accounted for by the marker m. This expression of the color function provides a statistical value since the volume of phase p in the cell is

normalized by the volume represented by all the particles inside the cell, and not by the volume of the cell itself. The normalization is compulsory, as the markers do not interact explicitly. Therefore, according to the velocity field, certain particles may overlap or a cell can contain more particles than n^3, inducing a volume lower or higher than the real volume of the cell.

This highlights one of the main features of the method regarding the mass conservation: the calculation of the color function is highly dependent on the markers' density, and especially on their proportion according to the function ϕ_m^p. Indeed, a marker isolated in one cell may result in a color function of 1 just because there is no other marker to balance its phase function ϕ_m^p. In order to avoid this numerical artefact, one should redistribute the markers exiting the computational domain into rarefied cells.

2.2.4. Redistribution of the particles

According to the streamlines of the flow, the particles can converge or diverge from one area to another. In this way, certain Eulerian grid cells are free from particles at certain time steps. This phenomenon has been classically observed in particle numerical methods such as [3,9,25,7], in which various remeshing methods to redistribute the particles over time have been proposed.

Here, we choose to favor the mass conservation property to redistribute the particles. Indeed, in all the investigated simulations, empty Eulerian cells were encountered in simulation problems where inlet and outlet boundary conditions were stated. In these configurations, the total number of particles initially lying in the computational domain is *a priori* not constant over time. The mass conservation is ensured by injecting particles in boundary cells where an inlet boundary condition is imposed, or by redistributing the particles exiting the computational domain at the outlet into cells containing the smaller number of particles. A specific variable *Lim* is defined to characterize the property of each Eulerian cell with respect to the boundary position Γ or the interior of Ω. The boundary Γ is made of 6 (4 in two-dimensions) boundary parts $\Gamma_{left}, \Gamma_{right}, \Gamma_{bottom}, \Gamma_{top}, \Gamma_{behind}$ and Γ_{front} such as $\Gamma = \Gamma_{left} \cup \Gamma_{right} \cup \Gamma_{bottom} \cup \Gamma_{top} \cup \Gamma_{behind} \cup \Gamma_{front}$. We have:

$$
\begin{aligned}
&Lim_{i,j,k} = 1 \quad \text{if } x_{i,j,k} \in \Omega \text{ and } x_{i,j,k} \in \Gamma \\
&Lim_{i,j,k} = 2 \quad \text{if } x_{i,j,k} \in \Gamma_{left} \\
&Lim_{i,j,k} = 3 \quad \text{if } x_{i,j,k} \in \Gamma_{right} \\
&Lim_{i,j,k} = 4 \quad \text{if } x_{i,j,k} \in \Gamma_{bottom} \\
&Lim_{i,j,k} = 5 \quad \text{if } x_{i,j,k} \in \Gamma_{top} \\
&Lim_{i,j,k} = 6 \quad \text{if } x_{i,j,k} \in \Gamma_{behind} \\
&Lim_{i,j,k} = 7 \quad \text{if } x_{i,j,k} \in \Gamma_{front}
\end{aligned}
$$

If it is assumed that a particle m belongs to Ω_i, j, k, i.e. the Eulerian control volume surrounding the Eulerian node (i, j, k), this particle is located according to its relative position to the boundaries as follows (see Section 2.2.2):

$$
\begin{aligned}
&\phi_m = \infty \quad \text{if } x_{i,j,k} \in \Gamma_{left} \text{ and } x_m < -0.5 \\
&\phi_m = \infty \quad \text{if } x_{i,j,k} \in \Gamma_{right} \text{ and } x_m > -0.5 \\
&\phi_m = \infty \quad \text{if } x_{i,j,k} \in \Gamma_{bottom} \text{ and } y_m < -0.5 \\
&\phi_m = \infty \quad \text{if } x_{i,j,k} \in \Gamma_{top} \text{ and } y_m > -0.5 \\
&\phi_m = \infty \quad \text{if } x_{i,j,k} \in \Gamma_{behind} \text{ and } z_m < -0.5 \\
&\phi_m = \infty \quad \text{if } x_{i,j,k} \in \Gamma_{front} \text{ and } z_m > -0.5
\end{aligned}
$$

All the particles marked by $\phi_m = \infty$ are redistributed in the cells where the particle number is the minimum at each time step. This procedure ensures that no empty cell is created during time. It is efficient in curvilinear coordinates as the redistribution procedure uses the position of the particles in the local transformed coordinate system (see Section 2.2.1).

3. Application of the VOF-SM method to scalar interface tracking problems

A set of test cases was used to study the ability of the method to accurately describe strongly distorted interfaces. Stretching and shearing stresses are of great importance in multiphase flows, and the major limitation of classical methods in accounting for small scales generated by those effects is the grid size. The following test cases aim at presenting the performances of the Lagrangian sub-grid description. The precision and the performance of the method are quantitatively validated by its ability to ensure mass conservation along the simulation, as well as its capability of representing the concentration field as compared to a reference state. The initial state can be taken as the reference state if no exact solution is available. In this case, the accuracy is achieved through a time reverse procedure, which enables the calculation of the L1 error norm between this initial state and the final state, defined as

$$E_a = \sum_{(i,j,k)\subset\Omega} A_{i,j,k} |C^0_{i,j,k} - C^f_{i,j,k}| \tag{10}$$

Here, $A_{i,j,k}$ is the area (volume) of the cell (i, j, k) and $C^0_{i,j,k}$ and $C^f_{i,j,k}$ are respectively the initial and final values of the concentration field in $\Omega_{i,j,k}$. The order of convergence is deduced from the calculated errors by the expression: $\vartheta = \frac{ln(E(2N)/E(N))}{ln(1/2)}$ where

$E(N)$ and $E(2N)$ are the L1 error norm calculated with N and $2N$ Eulerian grid cells, respectively. The mass conservation accuracy is evaluated at each time step NT, through the calculation of the relative error of the total mass in the computational domain:

$$E_m = \left(\sum_{(i,j,k)\subset\Omega} A_{i,j,k} C^0_{i,j,k} - \sum_{(i,j,k)\subset\Omega} A_{i,j,k} C^{NT}_{i,j,k} \right) \Big/ \sum_{(i,j,k)\subset\Omega} A_{i,j,k} C^0_{i,j,k} \tag{11}$$

The physical time t is equal to $NT\delta t$, where δt is the time step.

3.1. Shearing of a circle in a vortex velocity field

This test case is referred to as the vortex in a box problem or reverse vortex flow. A solenoidal velocity field is imposed, stretching the fluid into a thin continuous spiral-shaped filament converging to the center of the domain. Initially, a circular area of fluid, 0.15 m in diameter, is located at the coordinates $(0.5, 0.75\ \mathrm{m})$ of a unit square computational domain. The prescribed velocity field is described by the periodic stream function

$$\Psi(x,y) = \frac{1}{\pi} sin^2(\pi x) sin^2(\pi y) cos(\pi t/T)$$

where T is the period of the velocity fluctuations. The initial circle exhibits the largest deformation at $t = T/2$, and returns to its initial position at $t = T$, at the end of the full calculation. The total mass of the computational domain can be compared to the initial mass along the calculation while the L1 error norm compares the initial and final concentration fields.

The effect of the particle number per cell as well as the influence of the CFL condition are investigated in terms of accuracy and mass conservation, with a regular and an irregular grid.

3.1.1. Regular mesh

For the lowest number of particles, i.e. four particles per cell (ppc), and a CFL condition of 1, based on the maximum velocity in the domain, the method exhibits an order of accuracy higher than 2, and error levels nearly one order of magnitude lower than [4] with a particle method, and at least two orders of magnitude lower than [33] with an improved VOF approach (Fig. 5). The order of accuracy is conserved when increasing the number of particles from 2 to 4 per direction per cell and diminishing the CFL-condition from 1 to 0.1 (Fig. 6).

The L1 error norm is highly dependent on the CFL-condition, whereas the number of particles weakly influences the accuracy, especially at a low CFL-condition. For a given grid size, the CFL-condition defines the accuracy of the time discretization. At each iteration of the global resolution algorithm, the same velocity field is interpolated along the internal sub-steps of the

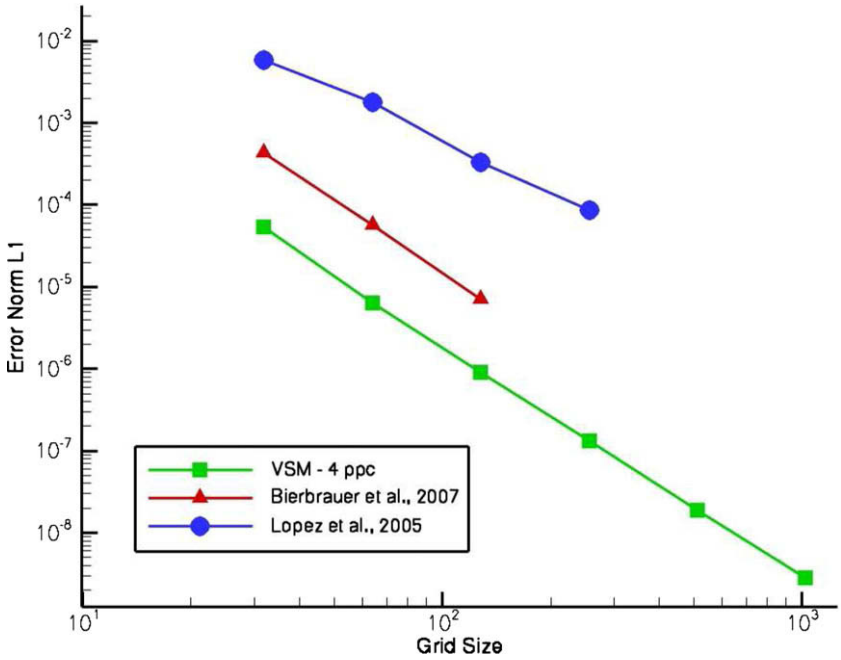

Fig. 5. Advection of a circular concentration field in a vortex velocity field on a regular grid – absolute error E_a versus grid size compared with previous studies of [33] and [4] – CFL = 1 and 4 ppc .

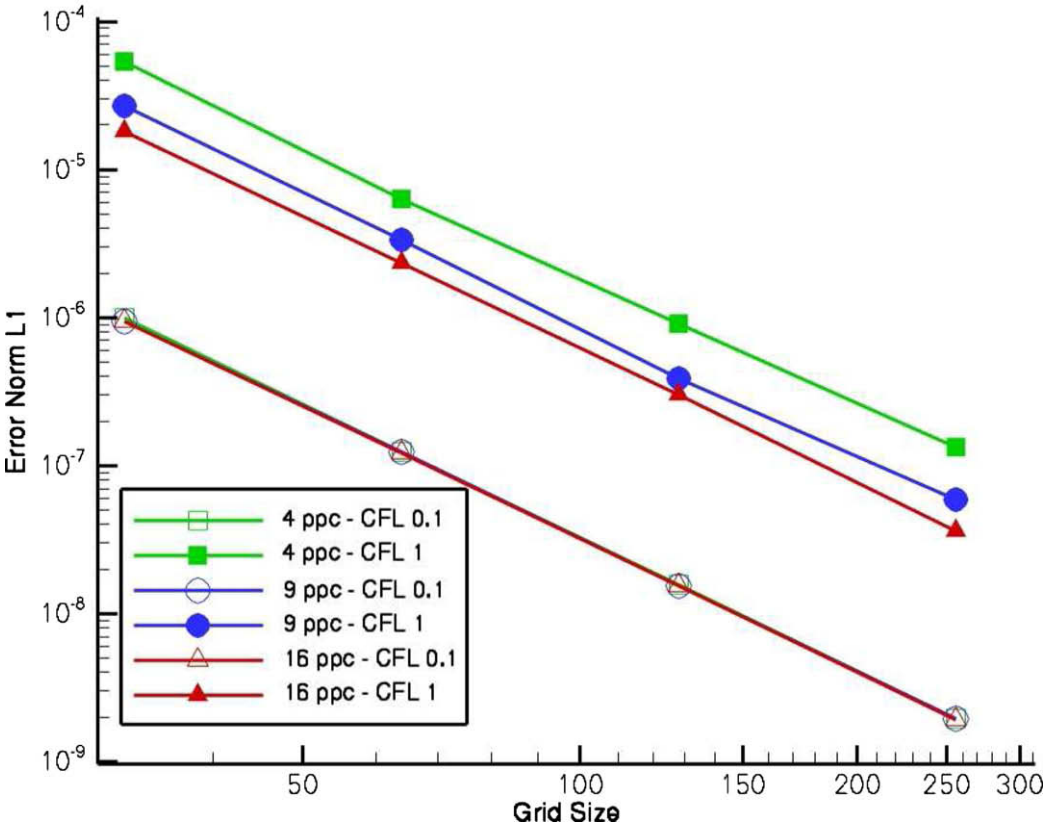

Fig. 6. Advection of a circular concentration field in a vortex velocity field on a regular grid – absolute error E_a versus grid size for several particle densities and CFL conditions.

Table 1
Advection of a circular volume fraction field in a vortex velocity field – absolute error E_a obtained with several numbers of particles per cell – CFL = 1 and 128^2 grid.

ppc	E_a error norm
4	9.083767898927395E−007
9	3.915566659799275E−007
16	2.986757099972148E−007
25	2.424825734140292E−007

VOF-SM method. Consequently, the error introduced in the transport of the markers increases with the CFL-condition. For a sufficiently low CFL-value, the number of internal sub-steps equals one regardless of the initial particle density (from 4 to 16 ppc) and the error introduced by the velocity interpolation is independent of the ppc number. This justifies the superposition of the convergence curves when CFL = 0.1.

As shown in Table 1, the decrease of the L1 error gradually drops with an increasing number of particles per cell, thus indicating that the effect of the particle number becomes saturated. Inversely, the method exhibits an order higher than 2 for the convergence in time (Table 2).

Above a grid spacing of 1/64, in the 4 ppc case, the relative error on the total mass reaches levels lower than 1 (Fig. 7). The mass conservation property is enhanced by an increasing number of particles per cells (Fig. 8), whereas it is poorly affected by the CFL-condition (Fig. 9). The influence of the initial particle number in each cell is related to the way the color function is calculated (cf Section 2.2.3): a cell containing particles at $\phi_m = 1$ can be a full liquid cell or an interfacial cell. If it does not contain any particle at $\phi_m = 0$, the calculated color will be 1, and this absence of particles, i.e. $\phi m = 0$, can be due either to an artificial particle rarefaction effect, driven by the velocity field, or to a physical effect.

3.1.2. Irregular mesh

In practical applications, the computational domain is often discretized according to an irregular mesh, presenting coarse and fine areas, adapted to complex geometries or physical specificities such as boundary or mixing layers encountered, for

Table 2
Advection of a circular volume fraction field in a vortex velocity field – absolute error E_a obtained with several CFL conditions – 4 ppc and 128^2 grid.

Method	E_{conc}	E_C
VOF-SM	3.6477e−10	0
TVD	1.8497e−3	0.1801
WENO	1.3399e−3	0.1018

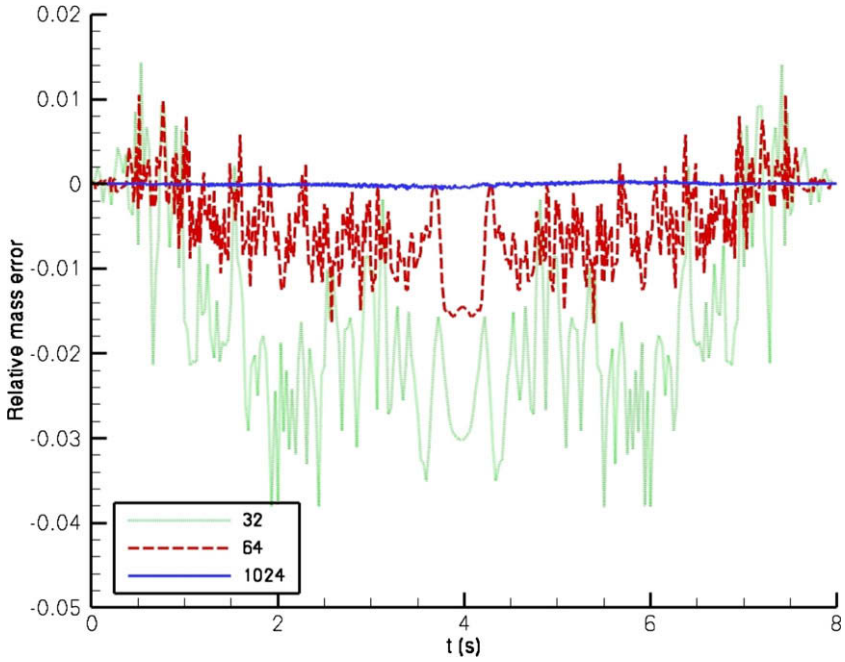

Fig. 7. Advection of a circular concentration field in a vortex velocity field on a regular grid – error E_m on the total mass versus time for several grid sizes – CFL = 1 and 4 ppc.

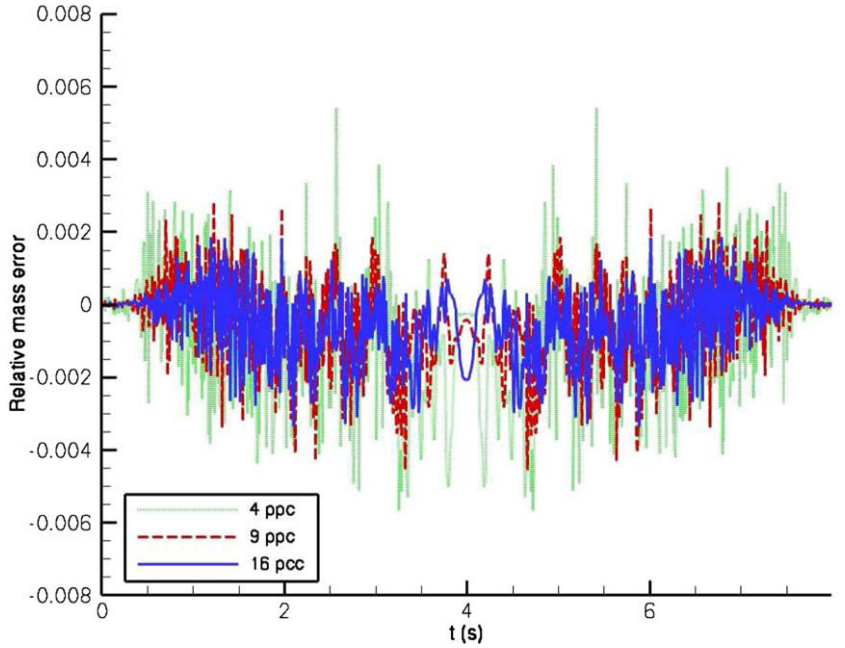

Fig. 8. Advection of a circular concentration field in a vortex velocity field on a regular grid – error E_m on the total mass versus time for several particle densities – CFL = 1 and 128^2 grid.

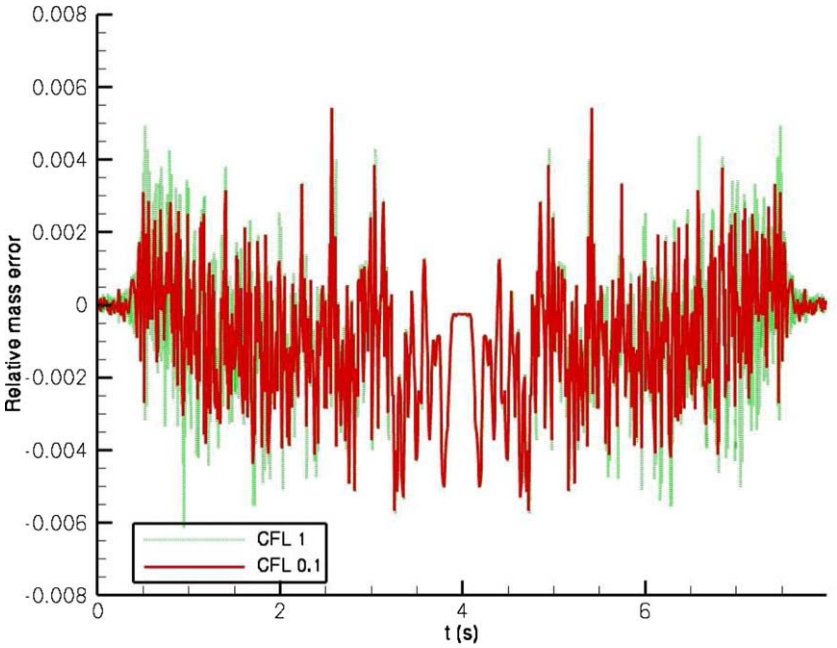

Fig. 9. Advection of a circular concentration field in a vortex velocity field on a regular grid – error E_m on the total mass versus time for several CFL conditions – 128^2 grid and 4 ppc .

instance, in fuel injection issues. The ability of the method to account for interface transport and distortions in such situations is investigated in the reverse vortex flow problem, through a specific grid presenting both fine and coarse areas, regularly arranged as shown in Fig. 10 for a 128^2 grid. According to Fig. 11, the influence of particle density on the accuracy is similar to the regular mesh case, however a different behavior is observed for the CFL parameter, which not only affects the precision but also the order of accuracy (Fig. 12). The decrease in order with an increasing CFL-condition is related to the number of internal sub-steps in the method. Indeed, a change in the CFL-value from 0.1 to 0.2, implies an increase in the iteration number from 1 to 2, whereas the decrease in the order occurs precisely between those values.

As for the regular mesh case, the CFL-condition only weakly affects the mass conservation along the simulation (Fig. 13). Inversely, the influence of the particle density is higher in the irregular case, as shown in Fig. 14: the increase in the total mass observed for 4 ppc, due to a lack of particles, vanishes with 16 ppc.

3.2. Shearing of a sphere in a vortex velocity field

The three-dimensional version of the method is investigated through the shearing of a sphere in a time periodic incompressible flow field combining a deformation in two perpendicular planes:

$$u(x,y,z) = 2sin^2(\pi x)sin^2(2\pi y)sin^2(2\pi z)cos(\pi t/T)$$
$$v(x,y,z) = -sin^2(2\pi x)sin^2(\pi y)sin^2(2\pi z)cos(\pi t/T)$$
$$w(x,y,z) = -2sin^2(2\pi x)sin^2(2\pi y)sin^2(\pi z)cos(\pi t/T)$$

Initially, the sphere is located at the position (0.35, 0.35, 0.35) in a unit computational domain, and its radius is 0.15 m. The mass variation is evaluated at each time step, and the accuracy is achieved by comparing the initial ($t = 0$ s) and the final ($t = T/2$) concentration fields, as in the 2D reverse vortex case. The period of the velocity fluctuations is $T = 3$ s.

The isosurface 0.5 of the color function is displayed in Fig. 15, for a 64^3 grid, 4 ppc and a CFL condition of 0.1, at the time $t = 0$ s,$t = 0.75$ s,$t = 1.125$ s,$t = 1.5$ s,$t = 1.875$ s,$t = 2.25$ s and $T = 3$ s. As expected, the couples 0 s/3 s, 0.75 s/2.25 s and 1.125 s/1.875 s are identical. The convergence properties experienced on the reverse vortex flow are also exhibited in this 3D case. The maximum deformation that occurs at $t = T/2$ induces an increase of 2% in the total volume for 9 ppc on a 64^3 grid, which is similar to the results obtained by [13] with a hybrid particle level-set method on a 100^3 grid.

3.3. Deformation of a circle in a converging–diverging pipe

3.3.1. Cartesian grid simulations

A circular area of liquid is advected by an analytic solenoidal velocity field, in a converging–diverging channel. The two-dimensional velocity components are

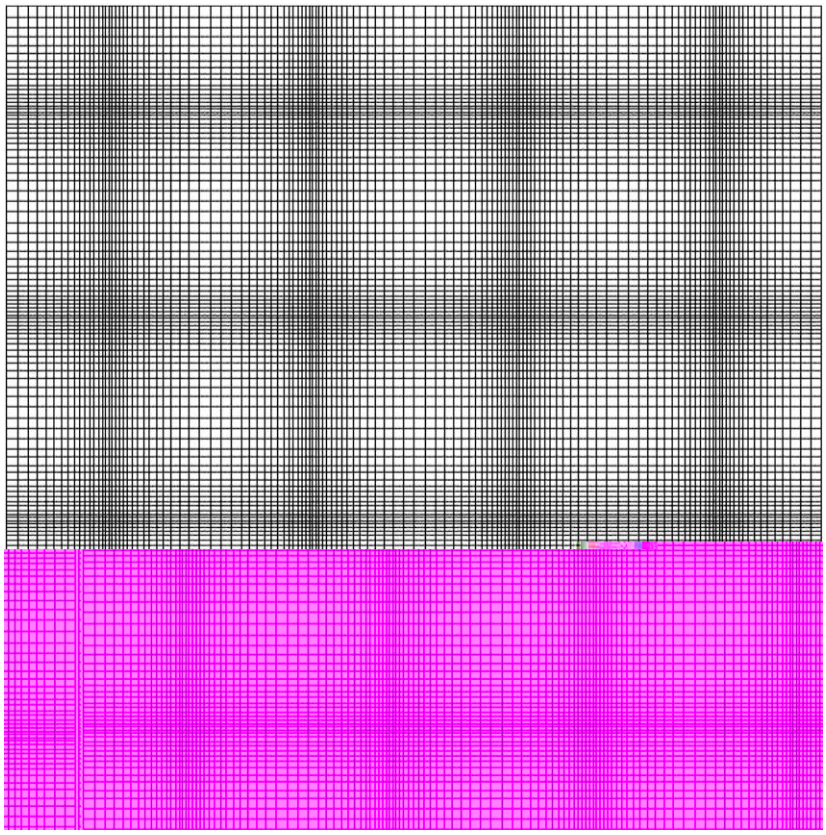

Fig. 10. An irregular mesh with 128^2 cells.

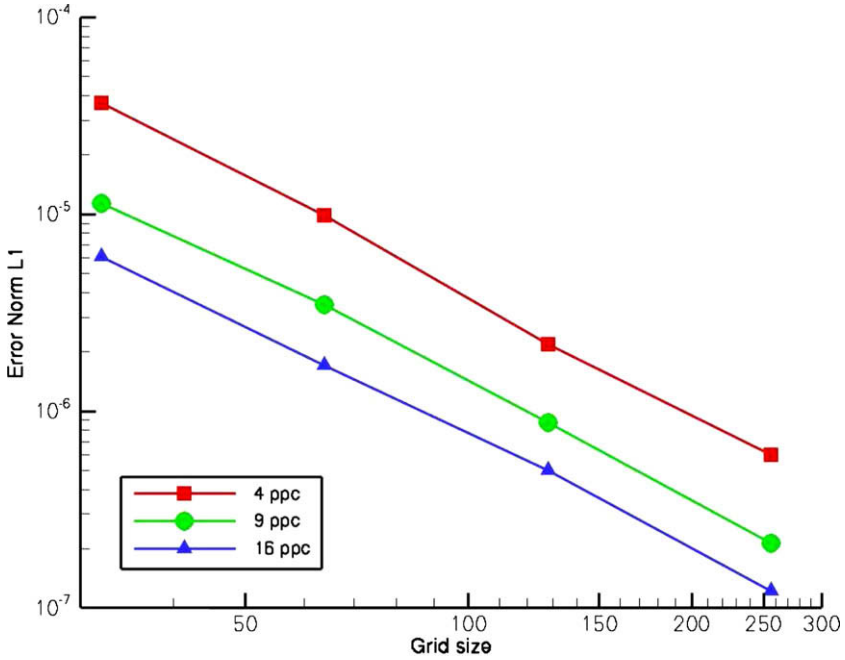

Fig. 11. Advection of a circular concentration field in a vortex velocity field on an irregular grid – absolute error E_a versus grid size for several particle densities – CFL = 1.

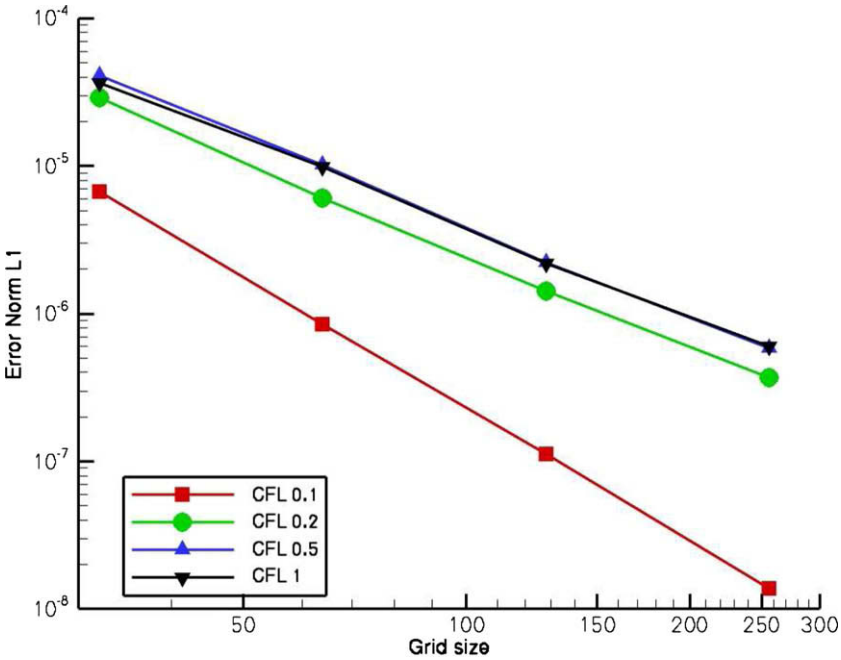

Fig. 12. Advection of a circular concentration field in a vortex velocity field on an irregular grid – absolute error E_a versus grid size for several CFL conditions.

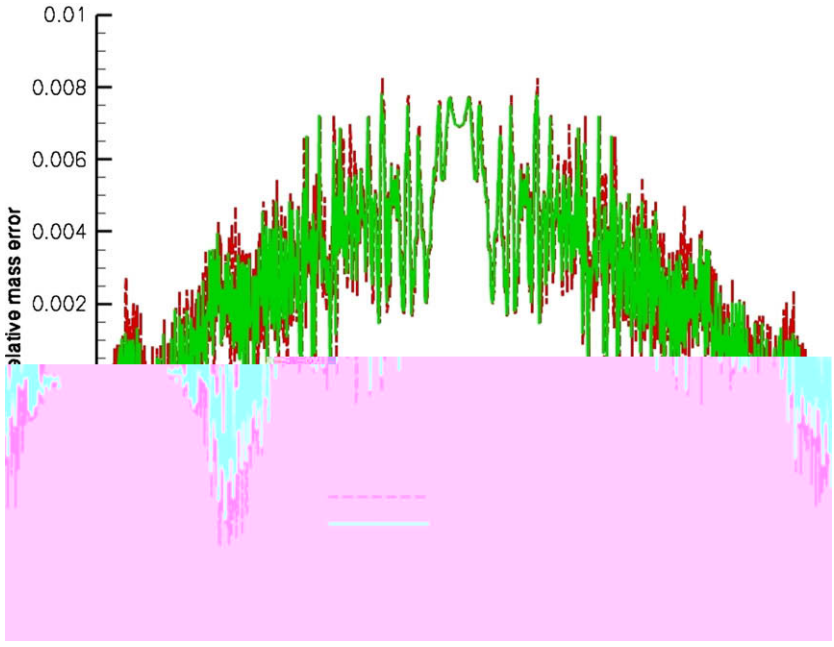

Fig. 13. Advection of a circular concentration field in a vortex velocity field on an irregular grid – error E_m on the total mass versus time for several CFLconditions – 128^2 grid and 4 ppc.

$$u(x,y) = \left[1 - \left(\frac{y}{f(x)}\right)^2\right]\frac{1}{f(x)} \quad \text{if } y < f(x) \tag{12}$$

$$u(x,y) = 0 \text{ otherwise} \tag{13}$$

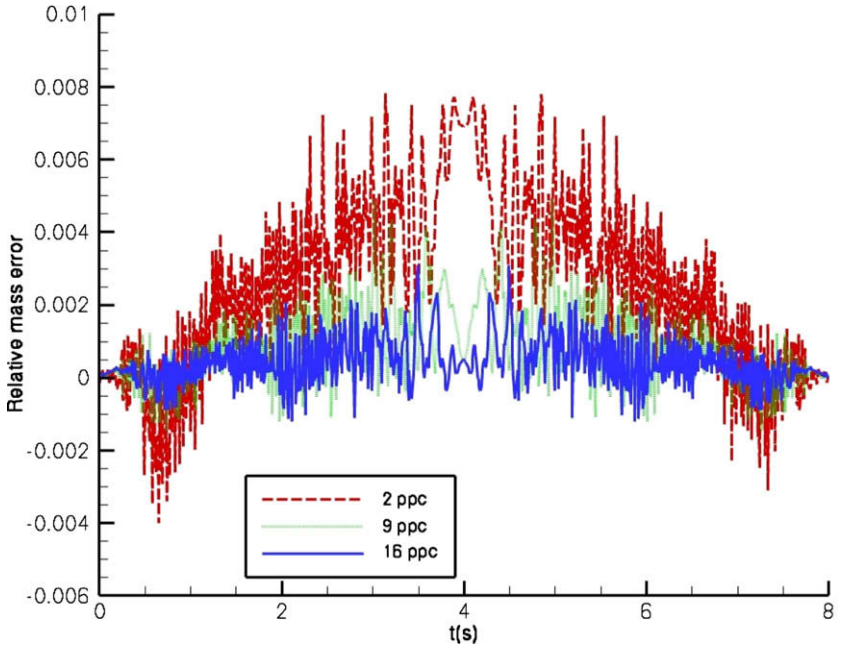

Fig. 14. Advection of a circular concentration field in a vortex velocity field on an irregular grid – error E_m on the total mass versus time for several particle densities – CFL = 1 and 128^2 grid.

and

$$u(x,y) = \left[1 - \left(\frac{y}{f(x)}\right)^2\right] \frac{y}{f(x)^2} \frac{d}{dx} f(x) \quad \text{if } y < f(x) \tag{14}$$

$$u(x,y) = 0 \text{ otherwise} \tag{15}$$

where $f(x) = 1 - \frac{3}{4} exp(-2x^2)$ is the shape function of the channel. The liquid is initially located at the position $(-1.95\text{ m}, 0\text{ m})$ of the computational domain presented in Fig. 16. This test case has already been investigated by [16]. They compared level-set and VOF simulations to front-tracking reference results on a 256×128 grid. The non-conservative behavior of the level-set solution provided a less accurate solution in the larger curvature zones of the interface as compared to the VOF method they used. The VOF-SM solution for a 256×128 grid is better than the VOF solution of [16]. Two characteristic times are considered in the comparisons, $t = 1.787109375\,s$ demonstrating a fish like shape of the interface and $t = 2.958984375$ s where a frisbee shape can be observed. The same time step as in [16] is used, $\Delta t = 0.00146484375$ s. The results of the VOF-SM approach are almost superimposed to the front-tracking reference solution at the two chosen times. The particles are plotted in Figs. 17 and 18, which illustrate the effect of the particle redistribution on an open-boundary case. Without redistribution, the particles are advected towards the outlet boundary and the domain is progressively emptied of particles. The redistribution step provides the emptied cells with the outgoing particles that are compulsory in order to account for problems such as injection.

3.3.2. Curvilinear grid simulations

The advection of an initial circular Volume Of Fluid function, presented in the previous section, is subsequently investigated on a curvilinear orthogonal grid, as presented in Fig. 19, with 128×64 grid points. The curvilinear meshes were generated with the open source software GridGen [17]. The grid lines followed the stream lines of the velocity field 12, 13, 14 and 15 such that:

$$u(\xi,\eta) = -\left(\left[(1 - \left(\frac{\eta}{F(\xi)}\right)^2)\frac{1}{F(\xi)}\right]^2 + \left[\left(1 - \left[\frac{\eta}{F(\xi)}\right]^2\right)\frac{3\xi\eta}{F(\xi)^2} exp(-2\xi^2)\right]^2\right)^{1/2}$$

$$v(\xi,\eta) = 0$$

where ξ and η are the curvilinear coordinates and $F(\xi) = 1 - \frac{3}{4} exp(2\xi^2)$. The curvilinear coordinates are comprised within the ranges $-2.5 \leqslant \xi \leqslant 2.5$ and $-F(\xi) \leqslant \eta \leqslant F(\xi)$.

The convergence of the VOF-SM method on curvilinear meshes was studied on three grids containing 256×128, 512×256 and 1024×512 discretization points. Three particles per direction and cell were used. The results of the comparisons are

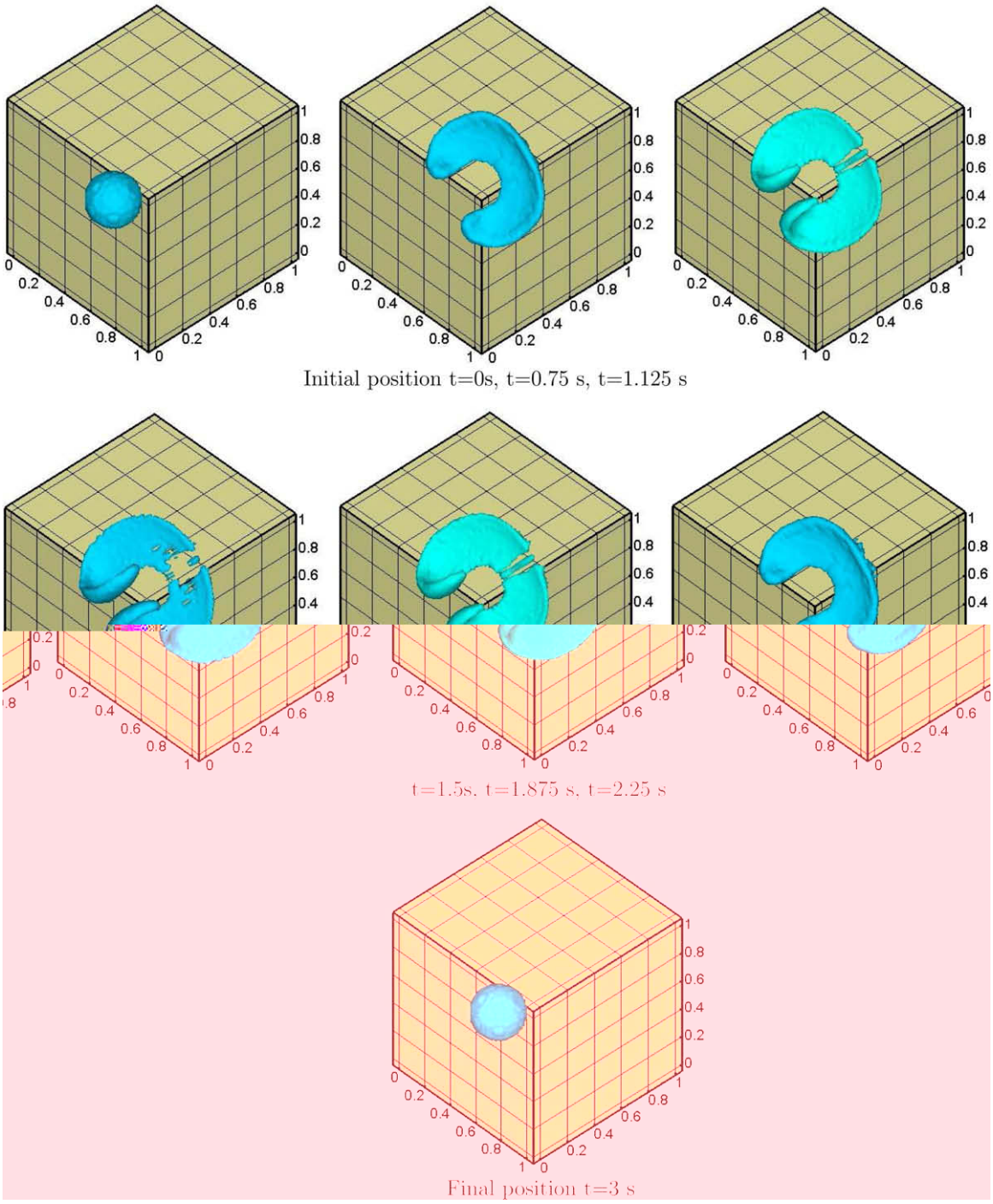

Fig. 15. Advection of a sphere in a vortex velocity field – isosurface $C = 0.5$—64^3 grid size and 9 ppc.

presented in Fig. 20. It can be observed that the VOF-SM simulations provided comparable solutions even on the coarser grid. At $t = 1.787109375$ s, small discrepancies are noticed in the middle of the tail of the fish-shaped interface whereas the larger gap at $t = 2.958984375$ s is localized at the right hand side of the frisebee interface shape. The curvilinear VOF-SM simulations are in very good agreement with the front-tracking reference results of [16]. If attention is paid to the relative accordance of the Cartesian and curvilinear VOF-SM simulations with the front-tracking data, it can be observed that on a 1024×512 grid, which is finer than the 256×128 Cartesian VOF-SM grid, the Cartesian VOF-SM simulations are sligtly superior to the curvilinear results. This fact is mainly due to the error made in the discretization and velocity interpolation of the VOF-SM method.

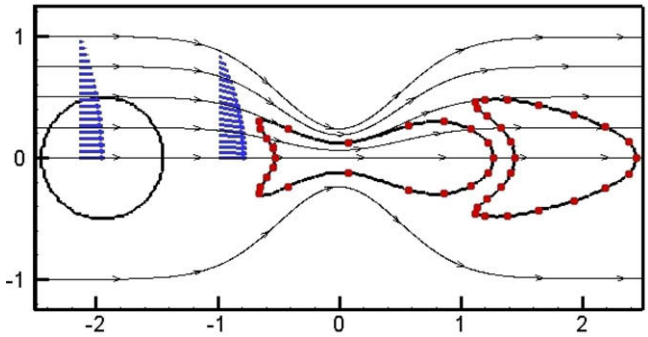

Fig. 16. Advection of a circular shape in a converging–diverging channel by a solenoidal velocity field. Comparison of the VOF-SM and front-tracking solutions [16] – CFL = 1 and 256 × 128 grid and 4 ppc.

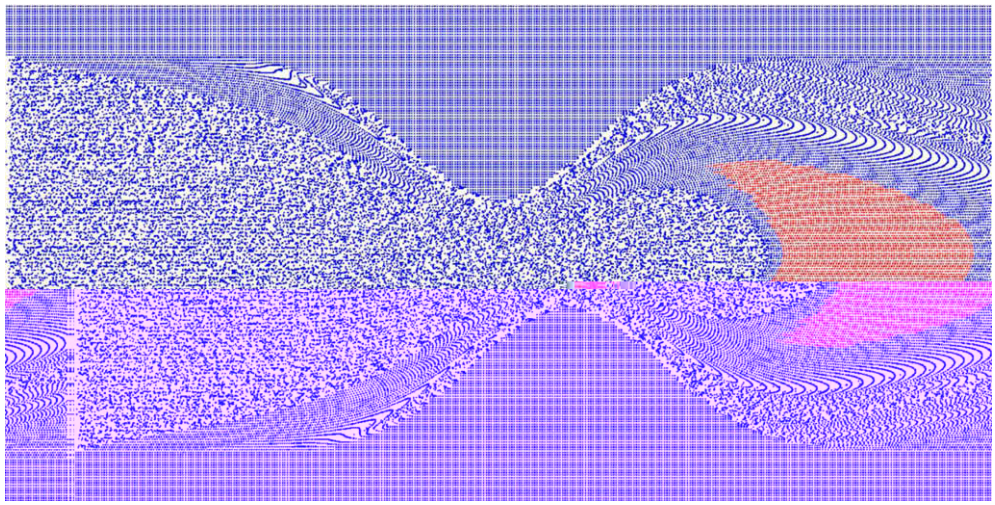

Fig. 17. Advection of a circular shape in a converging–diverging channel by a solenoidal velocity field. Particle distribution at $t = 2.96$ s with particle redistribution.

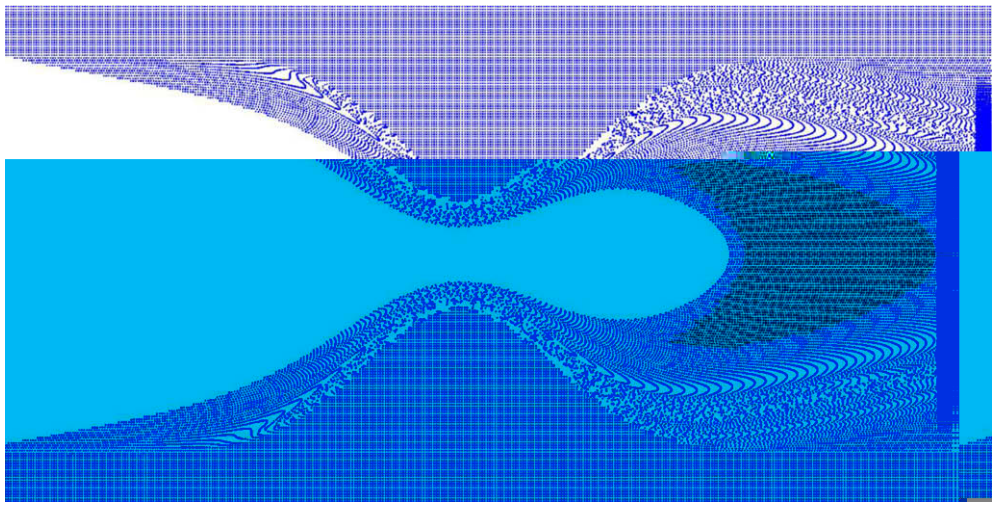

Fig. 18. Advection of a circular shape in a converging–diverging channel by a solenoidal velocity field. Particle distribution at $t = 2.96$ s without particle redistribution.

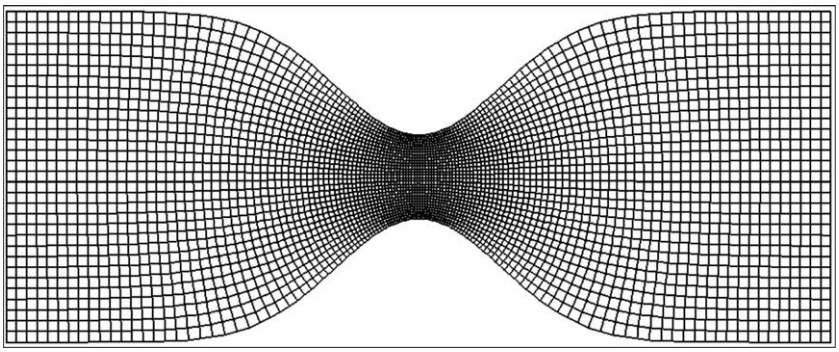

Fig. 19. Orthogonal curvilinear grid of the converging–diverging channel of [16] – 128 × 64 grid points.

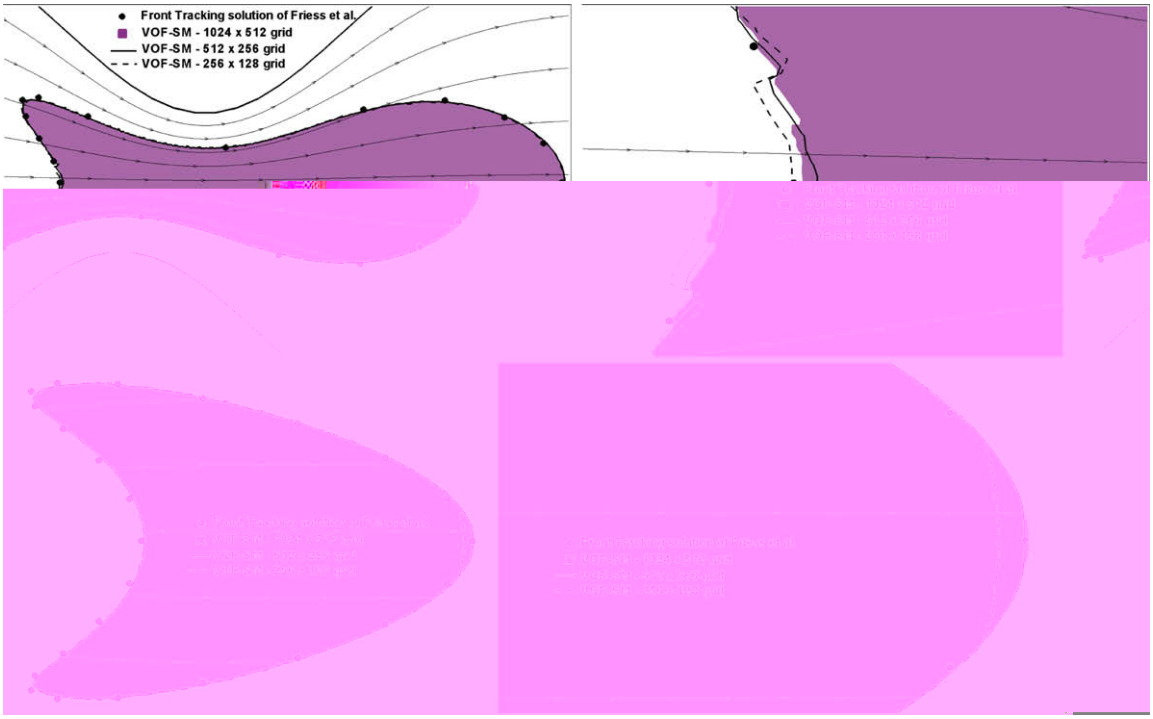

Fig. 20. Deformation of a circular interface in the converging–diverging channel of [16] – comparison between the curvilinear simulations on 256 × 128, 512 × 256 and 1024 × 512 grids for $t = 1.787109375$ s (top figures) and $t = 2.958984375$ s (bottom figures).

Indeed, the edges of the curvilinear cells are assumed linear, and in a global point of view, the curvilinear VOF-SM simulations are accurate. Similarly to the Cartesian simulations, the redistribution procedure of the particle is efficient in curvilinear grid simulations. The objective of this approach is to remain identical regardless of the orthogonal structured grid used. No specific discretizations or particle management are required in spherical, cylindrical or curvilinear grids as the VOF-SM method works in transformed coordinate systems.

4. Application of the VOF-SM method to scalar transport problems

The numerical simulation of the transport of a diffuse scalar quantity such as the concentration of a chemical specie, is classically modeled by the continuum Eq. (1) including a time derivative term, a hyperbolic advection term and a diffusive term. Many research efforts have been devoted to the discretization and solution of this equation, since a large number of industrial and environmental applications are concerned with the local description of the concentration gradients. All the existing methods and numerical schemes induce artificial diffusion or spurious oscillations of the concentration field [36,37,55,38,12,20,11] or [5]. In this section, improvements brought on by the VOF-SM method are evaluated and compared to the previous numerical studies. Only the advection term of the transport equation is considered in this investigation.

4.1. Advection of a complex 1D concentration profile

The 1D test case of the advection with a constant velocity of a complex concentration profile is considered first. The initial shape of C is composed of a Gaussian, a square, a triangular and an elliptical wave, as initially proposed by [22]. This problem is complex as it combines sharp features as well as regular characteristics of the concentration. The present test case has been widely used in the literature to validate the accuracy of discretization schemes devoted to the approximation of hyperbolic advection or transport equations [22,46,12]. The constant velocity is equal to 1 m s^{-1}, the 1D calculation domain is defined by $-1 \leqslant x \leqslant 1$ and the concentration profile reads:

$$C(x) = exp(-log(2)(x+0.7)^2/0.0009) \quad \text{if } -0.8 \leqslant x \leqslant -0.6$$
$$C(x) = 1 \quad \text{if } -0.4 \leqslant x \leqslant -0.2$$
$$C(x) = 1 - |10(x-0.1)| \quad \text{if } 0 \leqslant x\ 0.2$$
$$C(x) = \left(1 - 100(x-0.5)^2\right)^{1/2} \quad \text{if } 0.4 \leqslant x\ 0.6$$
$$C(x) = 0 \text{ otherwise}$$

Periodic conditions are imposed at the boundaries of the calculation domain. The numerical solution is compared to the analytical one, i.e. the initial solution, after 4 periods T. Concerning the VOF-SM method, the quality of the numerical solution is independent on the number of simulated periods, contrary to other approaches such as WENO or TVD schemes [12]. A CFL-number of 1 is considered in this section.

The evolution of the absolute error on concentration versus grid refinement is presented in Table 3 for the VOF-SM method, the Lax-Wendrof TVD scheme [28] and a 5th order WENO scheme [22]. This error E_{conc} is calculated as

$$E_{conc} = |C(x, t = 0s) - C(x, t = 3s = T)| \tag{16}$$

Regardless of the grid size, the VOF-SM method provides an almost zero computer error. The Lagrangian characteristic of the VOF-SM method induces no numerical diffusion and preserves the exact solution over time. On the contrary, the discretized TVD and WENO approaches do not preserve the initial shape of C and create spurious numerical diffusion or distortion of

Table 3
One-dimensional advection of a complex concentration field – absolute error E_{conc} versus grid size obtained with the VOF-SM, TVD and WENO methods.

Grid	VOF-SM	TVD [28]	WENO RK3 [22]
16	1.57e−15	0.91e+0	0.89e+0
32	1.62e−15	0.89e+0	0.86e+0
64	1.95e−15	0.57e+0	0.39e+0
128	1.97e−15	0.15e+0	0.15e+0
256	1.97e−15	8.48e−2	6.32e−2
512	1.98e−15	5.51e−2	2.72e−2

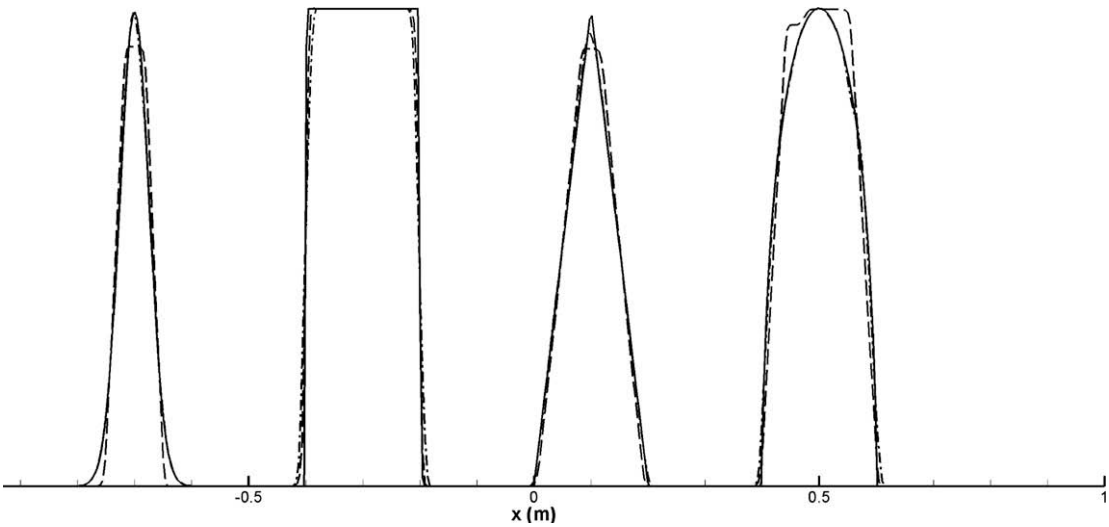

Fig. 21. Simulation of the transport of a complex 1D concentration field – comparison between the VOF-SM (line), TVD (dotted-dashed line) and WENO (long dashed line) approaches on a 512 grid.

the concentration field. These behaviors are illustrated in Fig. 21. They have also been observed with other approximation schemes based on spectral discretizations [36], Piecewise Polynomial methods (PPM) or Piecewise Rational Methods (PRM) [55].

4.2. Advection of a concentration profile in a vortex velocity field

The two-dimensional transport of a concentration cone is now considered in a vortex without deformation. This test case is similar to the rotating cosine hill used, for instance, by [36], however, it is more difficult as the cone shape is sharper than the cosine hill. In a 1-m square calculation domain, the initial concentration profile reads

$$C(x) = \frac{0.15 - R}{0.15} \quad \text{if } R \leqslant 0.15$$
$$C(x) = 0 \text{ otherwise}$$

where $R = ((x-0.5)^2 + (z-0.25)^2)^{1/2}$. The vortex velocity fields is expressed as

$$\mathbf{u}_x = -\frac{\pi}{2}(z-0.5) \tag{17}$$

$$\mathbf{u}_z = \frac{\pi}{2}(x-0.5) \tag{18}$$

A new error E_C is estimated, which compares the value of the maximum of the cone at $t = 0$ s to its value after one advection turn:

$$E_C = |max(C(x, t=0)) - max(C(x, t=3))| \tag{19}$$

Table 4 presents the evolution of the error E_{conc} according to the mesh size and the CFL number. The results are obtained with the VOF-SM method and three particles per direction. An almost second-order convergence is observed regardless of the CFL-number, and the error can be slightly reduced by diminishing the CFL-number. However, E_{conc} remains practically the same when the time step is increased. By paying attention to the conservation of the maximum of the cone after one turn through E_C in Table 5, it can be seen that the VOF-SM method almost perfectly conserves the maximum concentration value whereas classical approaches, such as the TVD or WENO schemes, induce a dramatic loss of the cone peak. The results obtained in this section are superior to those arising from simulations performed with other methods of the literature, such as spectral or spline-based schemes [36] or flux-corrected transport algorithms [20].

Fig. 22 presents the concentration profiles calculated with the VOF-SM, TVD and WENO approaches. The VOF-SM solution benefits from the Lagrangian character of the method and advects exactly the cone shape of the concentration. Contrarily, for this simple example, the Eulerian WENO and TVD schemes induce a loss of the cone maximum and a smoothing of the concentration profile in the peak zone.

4.3. Shearing of a cone in a shearing vortex velocity field

The deformation of a concentration cone in a vortex velocity field was investigated. This test case is difficult as the cone shape is strongly distorted in a first step, whereas, after one period of simulation, it returns to its initial shape. The initial concentration profile is identical to that in the previous test case, whereas the deformation vortex velocity fields is the same as the one used in Section 3.1.

Tables 6 and 7 present the absolute error E_{conc} and the space convergence order of the VOF-SM method according to the number of particles per direction and cell as well as to the CFL-number. An almost third order convergence rate is observed whatever the numerical conditions, which is in good agreement with the results obtained on interface tracking. Reducing the CFL number or the number of particles per cell leads to a weak reduction of E_{conc}. It can be concluded that the VOF-SM method remains very efficient for dealing with concentration profiles that interact with shearing velocity fields, such as turbulent flows for instance, even when large time steps and coarse distributions of particles are considered. By comparing the VOF-SM method to TVD and WENO scheme simulations in Table 8, it is possible to demonstrate that the VOF-SM method provides results that are almost 6 orders of magnitude better than the classical TVD and WENO approaches. The same conclusion

Table 4
Advection of a concentration cone in a vortex velocity field – absolute error E_{conc} versus grid size obtained with the VOF-SM method for several CFL-numbers after four turns – three particles are initially distributed in each space direction and in each cell.

Grid	CFL = 0.33	ϑ	CFL = 0.66	ϑ	CFL = 1	ϑ
16	9.0308e−5		1.0711e−4		1.0759e−4	
32	3.0444e−6	4.89	6.9955e−6	3.94	7.1784e−6	3.91
64	7.7136e−7	1.98	1.7728e−6	1.98	1.8191e−6	1.98
128	1.9356e−7	1.99	4.4487e−7	1.99	4.5650e−7	1.99
256	4.8436e−8	2.00	1.1140e−7	2.00	1.1430e−7	2.00

Table 5
Advection of a concentration cone in a vortex velocity field – values of $E_{co}n_c$ and E_C obtained with the VOF-SM, TVD and WENO methods after one turn – three particles are initially distributed in each space direction and in each cell – CFL = 1 and 64^2 grid.

Method	E_{conc}	E_C
VOF-SM	3.6477e−10	0
TVD	1.8497e−3	0.1801
WENO	1.3399e−3	0.1018

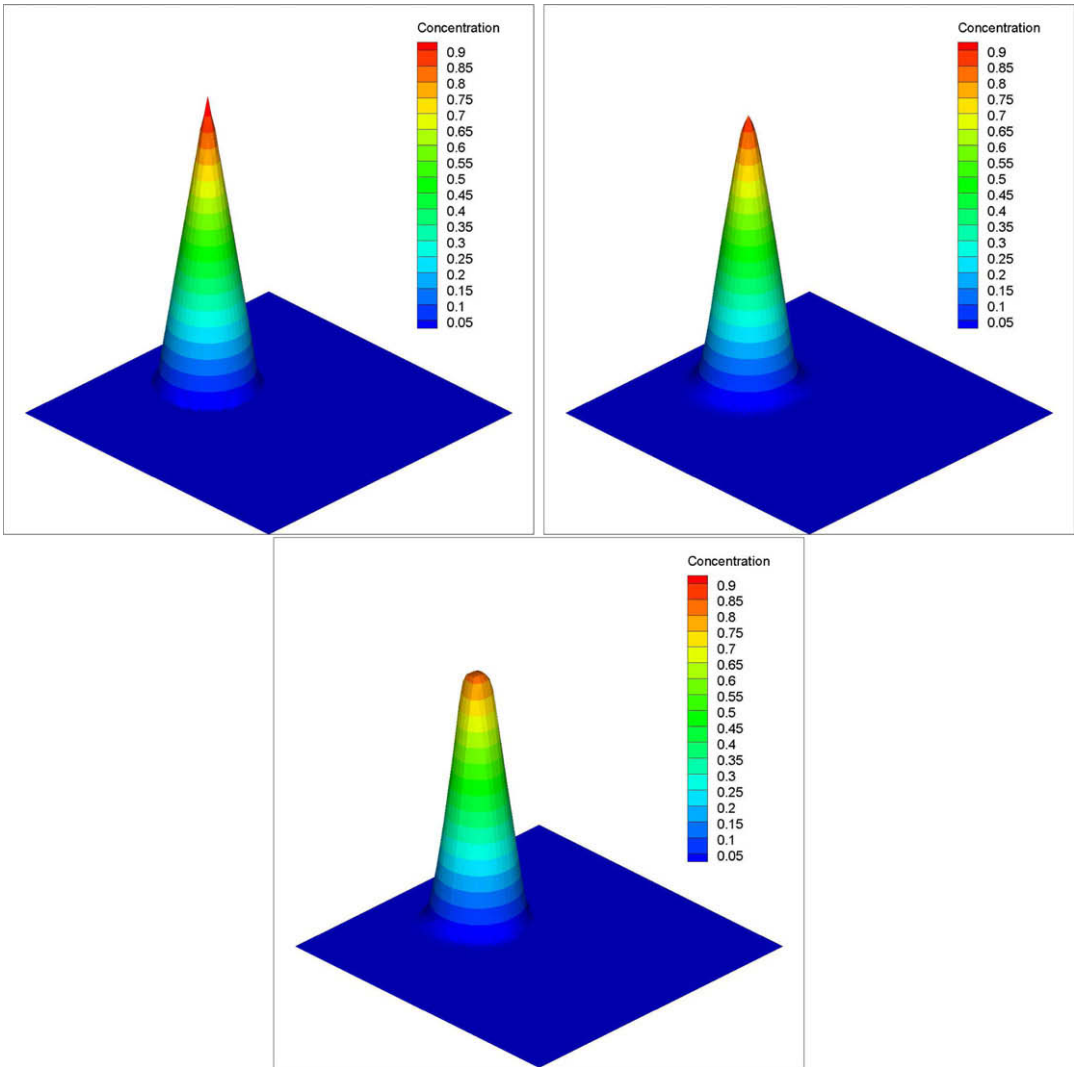

Fig. 22. Simulation of the transport of a cone in a vortex velocity field – comparison of 2D concentration profiles (extruded in 3D) between the VOF-SM,WENO and TVD methods from left to right on a 64^2 grid.

Table 6
Advection of a concentration cone in a shearing vortex velocity field – absolute error E_{conc} versus grid size obtained with the VOF-SM method for several CFL-numbers – two particles are initially distributed in each space direction and in each cell – $T = 8$ s in Eq. (12).

Grid	CFL = 0.33	ϑ	CFL = 0.66	ϑ	CFL = 1	ϑ
16	1.5571e−5		4.8865e−5		7.1459e−5	
32	1.5175e−6	3.36	5.3711e−6	3.19	8.3532e−6	3.10
64	1.9621e−7	2.95	3.3205e−7	4.02	1.1775e−6	2.83
128	2.4747e−8	2.99	1.0124e−7	1.71	1.4759e−7	3.00
256	3.1212e−9	3.00	1.2769e−8	2.99	1.8873e−8	2.97

Table 7
Advection of a concentration cone in a shearing vortex velocity field – absolute error E_{conc} versus grid size obtained with the VOF-SM method for several CFL-numbers – three particles are initially distributed in each space direction and in each cell – $T = 8$ s in Eq. (12). Advection of a concentration cone in a shearing vortex velocity field – absolute error E_{conc} versus grid size obtained with the VOF-SM method for several CFL-numbers – three particles are initially distributed in each space direction and in each cell – $T = 8$ s in Eq. (12).

Grid	CFL = 0.33	ϑ	CFL = 0.66	ϑ	CFL = 1	ϑ
16	8.6257e−6		5.7282e−5		5.1089e−5	
32	1.1587e−6	2.90	4.3713e−6	3.71	6.9203e−6	2.88
64	1.4793e−7	2.97	6.0580e−7	2.85	8.9201e−7	2.96
128	1.8597e−8	8.39	8.3935e−8	2.85	1.1598e−7	2.94
256	2.3272e−9	3.00	1.0007e−8	3.07	1.3828e−8	3.07

Table 8
Advection of a concentration cone in a shearing vortex velocity field – values of E_{conc} and E_C obtained with the VOF-SM, TVD and WENO methods – three particles are initially distributed in each space direction and in each cell – CFL = 1 and 64^2 grid – $T = 2$ s in Eq. (12).

Method	E_{conc}	E_C
VOF-SM	1.8493e−8	1.7881e−7
TVD	2.7737e−2	0.7580
WENO	2.6694e−2	0.7314

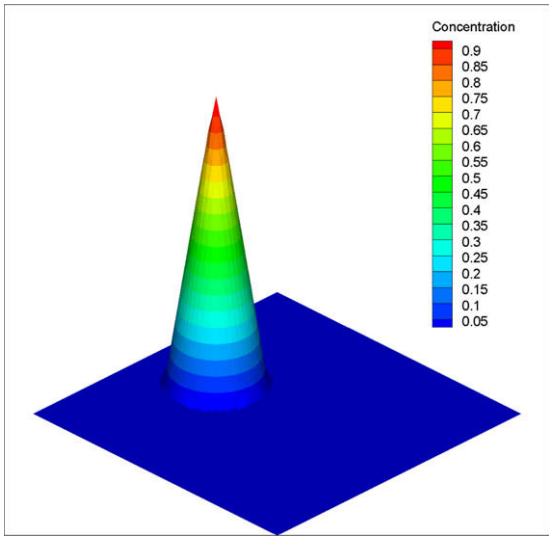

Fig. 23. Simulation of the transport of a cone in a deformation velocity field – initial condition of the 2D concentration profile (extruded in 3D) on a 64^2 grid.

applies to other methods of the literature [36] such as the quintic spline interpolation QSTSE method that has been investigated on a similar test case called deformative flow of Smolarkiewicz. In simulations with QSTSE, Nguyen and Dabdub [36] obtained an error $E_C = 0.1749$, comparable to the one provided by the TVD and WENO schemes. This error is again six orders of magnitude larger than the one obtained with VOF-SM.

The initial concentration profile used for the simulations, extruded in three dimensions, is plotted in Fig. 23. The range and shape of the concentration values are similar to those in the case of the vortex velocity field. After half a period, the initial cone became strongly distorted (see Fig. 24) ressembling a spiraling snake. It could be observed that the TVD and WENO scheme did not preserve the sharpness of the concentration and induced an important numerical diffusion, due to velocity gradients. On the contrary, the VOF-SM method preserves a more compact concentration field, with maximum values that are higher than those obtained with the TVD and WENO schemes. Fig. 25 presents the extruded 3D concentration results after one period. Theoretically, the initial condition must be recovered after 1 turn. The VOF-SM method achieves this property almost perfectly, with absolute and peak maximum errors of 10^{-8} and 10^{-7}. Contrarily, the TVD and WENO schemes have induced irreversible modifications of the stretched cone, under numerical diffusion effects. Dramatic differences are observed between the initial cone shape and the simulations provided by these classical approaches.

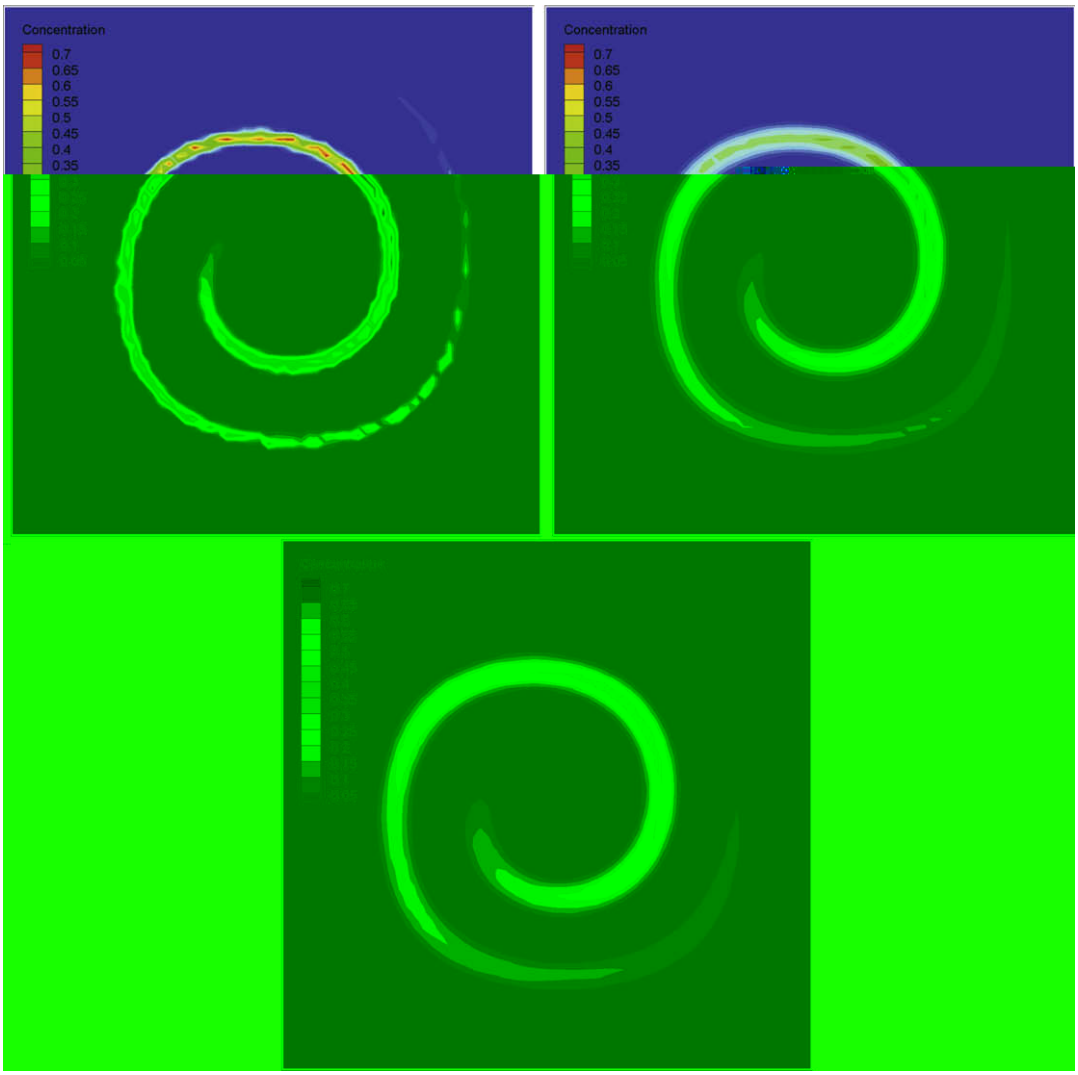

Fig. 24. Simlation of the transport of a cone in a vortex velocity field – comparison of 2D concentration profiles, after half a period, between the VOF-SM, WENO and TVD methods, from left to right and top to bottom, on a 64^2 grid.

4.4. Treatment of diffusion and 3D extensions

The point of building an accurate numerical method such as the VOF-SM for dealing with the advection part of a transport equation is to be able to simultaneously treat the diffusion of the concentration. Several methods exist to achieve it, based either on splitting techniques or direct approximations of the entire transport equation [37]. This point is not addressed in the present article but will be considered in future studies dedicated to the VOF-SM method.

Concerning the three-dimensional simulation of the transport of a concentration, the VOF-SM method complied with similar results as those presented in the sections devoted to interface tracking problems. The same qualities were observed, i.e. no numerical error arose with pure advection velocity fields whereas low diffusion and artificial deformation effects were measured when deformation fields were concerned. The results compared favorably to existing TVD or WENO schemes, similarly to what was demonstrated in two dimensions in previous sections.

5. Simulating free-surface flows with the VOF-SM method

The abilities of the VOF-SM method to simulate incompressible free surface flows are reported in this section. The VOF-SM approach is coupled to an augmented-Lagrangian Navier–Stokes solver that is efficient in the presence of variable density and viscosity fields. This numerical modeling has been detailed and validated by the authors in previous articles dedicated to laminar and turbulent two-phase flows [49,50,52,27,26,54]. Two classical free-surface flows are considered related to a 2D

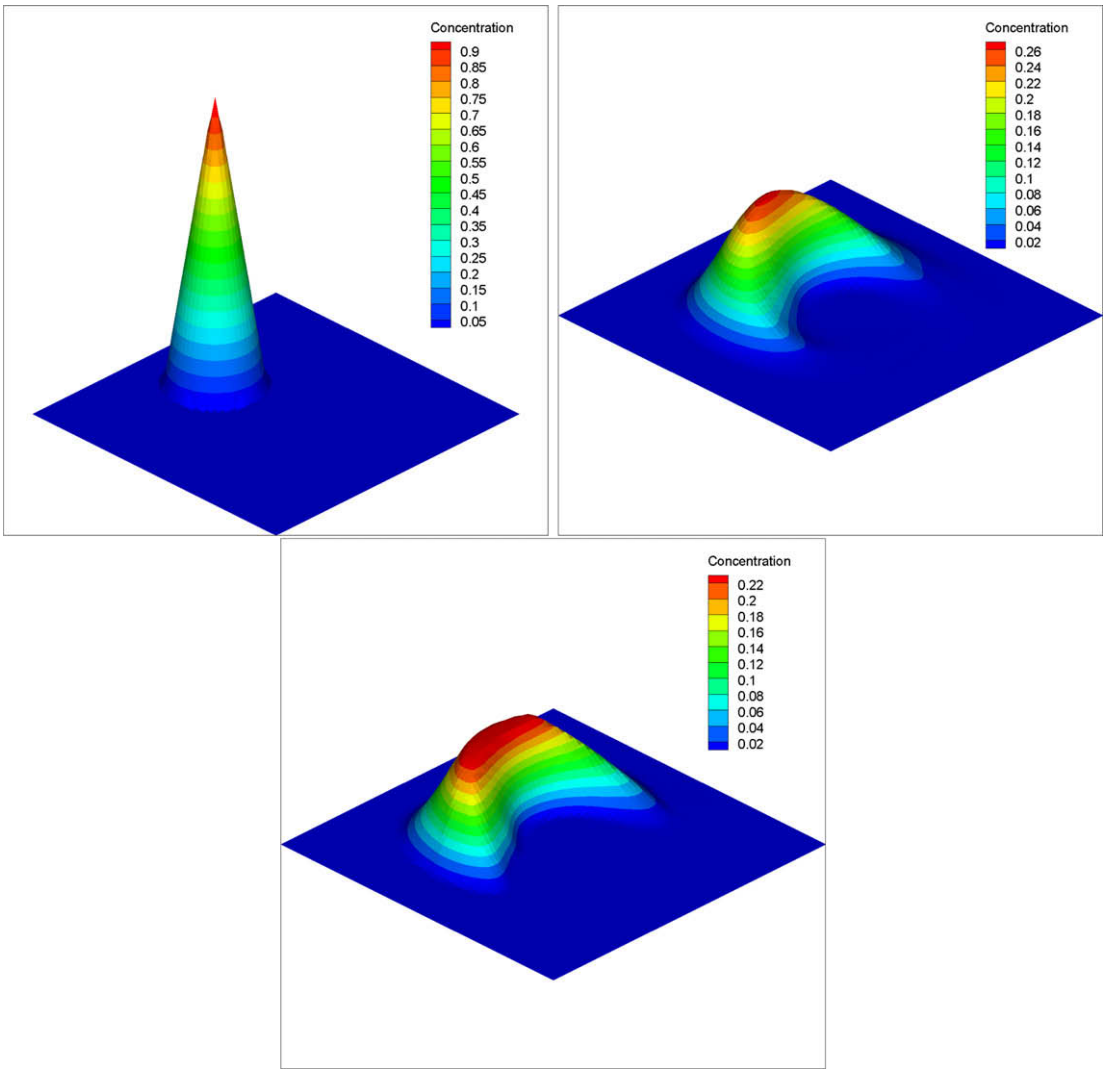

Fig. 25. Simulation of the transport of a cone in a vortex velocity field – comparison of 2D concentration profiles (extruded in 3D), after one period, between VOF-SM, WENO and TVD methods, from left to right and top to bottom,on a 64^2 grid.

Table 9
Characteristics of the fluids for the filling of a cavity by a viscous jet.

	ρ	μ
Viscous polymer	1000 kg m^{-3}	1000 Pa s
Air	1.1768 kg m^{-3}	1.85 10^{-5} Pa s

jet buckling in a square cavity and a three-dimensional dam-break flow in a tank. These problems are interesting in order to validate the numerical simulations as they are related to experiments or analytical studies.

5.1. Two-phase flow model

In the Eulerian approach, it is important to distinguish various media (gas or liquid) present in the calculation domain in order to accurately model incompressible two-phase flows. A characteristic or color function ϕ, i.e. the Volume Of Fluid function [19], allows to locate a variety of fluids thanks to an advection equation on the presence functions ϕ defined in Section 1. The interface between two media is defined as $\phi = 0.5$. Classically, the numerical model for an isothermal incompressible flow, called single-fluid or one-fluid model [43], reads :

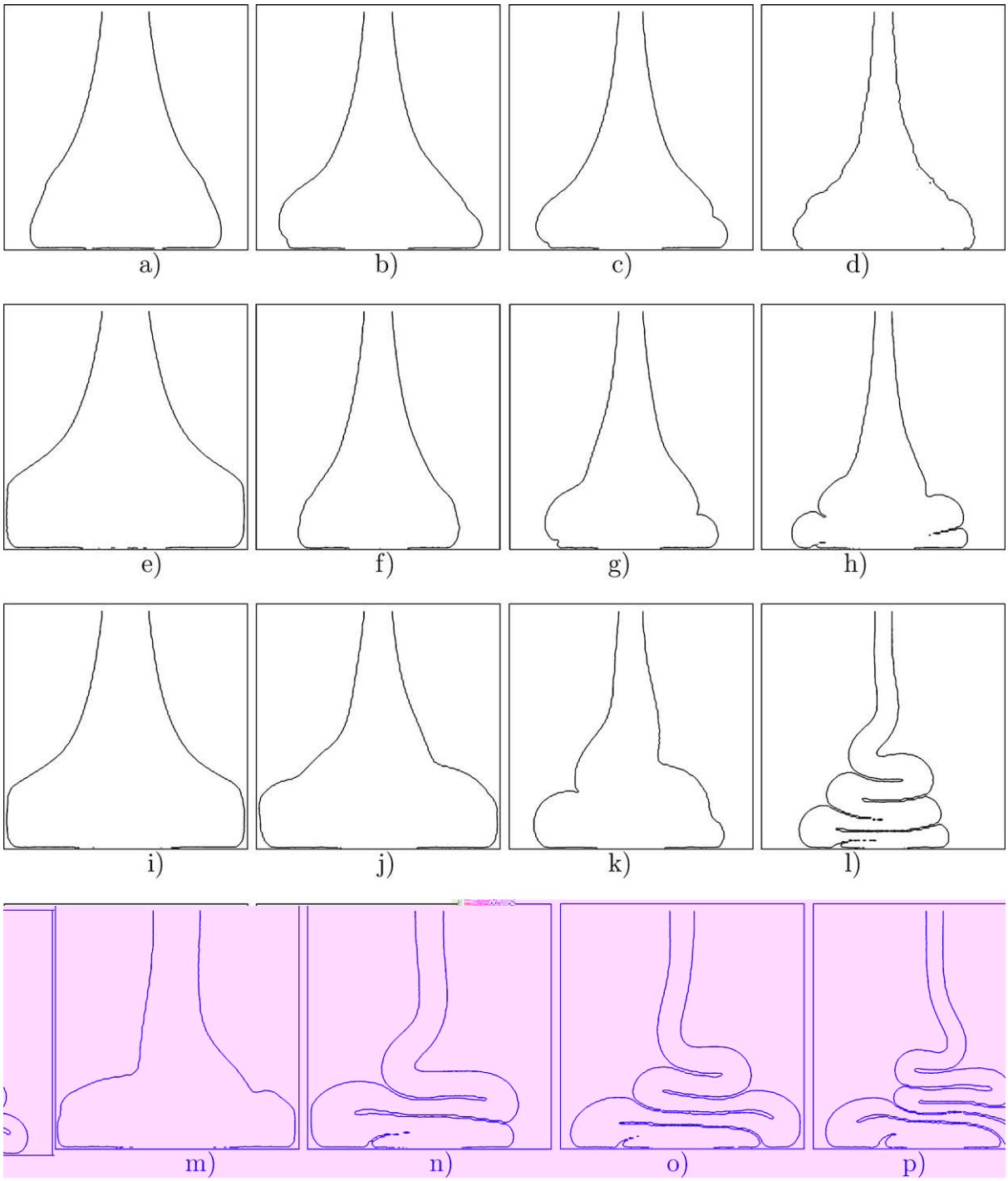

Fig. 26. Injection of a viscous fluid in a cavity – isocontour $C = 0.5$ – $Re = 0.6$: $H/D = 5$ and $t = 0.76$ s (a), $H/D = 9$ and $t = 0.62$ s (b), $H/D = 10$ and $t = 0.58$ s (c), $H/D = 15$ and $t = 0.48$ s (d), $Re = 0.5$: $H/D = 5$ and $t = 1.15$ s (e), $H/D = 9$ and $t = 0.64$ s (f), $H/D = 10$ and $t = 0.64$ s (g), $H/D = 15$ and $t = 0.54$ s (h), $Re = 0.3$: $H/D = 5$ and $t = 1.8$ s (i), $H/D = 9$ and $t = 1.5$ s (j), $H/D = 10$ and $t = 1.17$ s (k), $H/D = 15$ and $t = 0.75$ s (l), $Re = 0.1$: $H/D = 5$ and $t = 4.4$ s (m), $H/D = 9$ and $t = 3.0$ s (n), $H/D = 10$ and $t = 3.1$ s (o), $H/D = 15$ and $t = 2.5$ s (p), 128^2 grid and 9 ppc.

$$\rho\left(\frac{\partial \mathbf{u}}{\partial t} + \nabla \cdot (\mathbf{u} \otimes \mathbf{u})\right) = -\nabla \rho + \rho \mathbf{g} + \nabla \cdot \left[\mu(\nabla \mathbf{u} + \nabla^{\mathbf{t}} \mathbf{u})\right] \tag{20}$$

$$\nabla \cdot \mathbf{u} = 0 \tag{21}$$

$$\frac{\partial \phi}{\partial t} + \mathbf{u} \cdot \nabla \phi = 0 \tag{22}$$

$$\rho = \rho_1\phi + (1-\phi)\rho_0 \tag{23}$$
$$\mu = \mu_1\phi + (1-\phi)\mu_0 \tag{24}$$

where ρ and μ are the density and the viscosity of the single fluid, respectively, formulated in terms of the local characteristic function ϕ, t is the time variable, $\mathbf{u}$ the velocity, p the pressure and g the gravity. The density and viscosity in the liquid and gas fluids forming the free-surface flow are, respectively, defined as ρ_1 and μ_1 for the liquid and ρ_0 and μ_0 for the gas. The surface tension forces are not considered in this work. However, numerous investigation in the literature exist which include their effects as a volume force in the momentum equations [6].

5.2. Numerical methods dedicated to flow solver

An augmented Lagrangian approach was implemented to treat the coupling between the pressure and the velocity in the mass and momentum conservation Eq. (24) (Fortin and Glowinski [15], Vincent et al. [50,52,53]). This technique is based on a minimization algorithm in which a pressure–velocity saddle point is solved. An Uzawa method was implemented to numerically resolve the optimization problem. Implicit finite volumes on a fixed Cartesian staggered grid were used to discretize the motion equations. The time derivatives were approximated by a first order Euler scheme whereas the spatial fluxes were interpolated by centered schemes of second order. The resulting linear system was solved in two dimensions by a direct LU-type solver (PARDISO [44]) and in three dimensions by an iterative procedure of bi-conjugate gradient for a non-symmetric matrix BiCGSTAB II [48], preconditioned with an incomplete Gauss factorization ILU [18]. All the numerical methods are available in the Computational Fluid Dynamics (CFD) library Aquilon, developed by the TREFLE laboratory.

5.3. Jet injection in a square cavity

As a first example, a newtonian highly viscous liquid jet filling a square box that is open in its upper part, and initially full of air, is considered. The liquid, i.e. a polymer, is injected at the top of the box and flows to the bottom, accelerated by gravity. The characteristics of the flow are summarized in Table 9. Several injection velocities U and diameters D are considered to illustrate the various possible jet behaviors and topologies during the filling of the cavity:

$0.1\ \mathrm{m\,s^{-1}} \leqslant U \leqslant 9\ \mathrm{m\,s^{-1}}$
$0.067\ \mathrm{m} \leqslant D \leqslant 0.2\ \mathrm{m}$

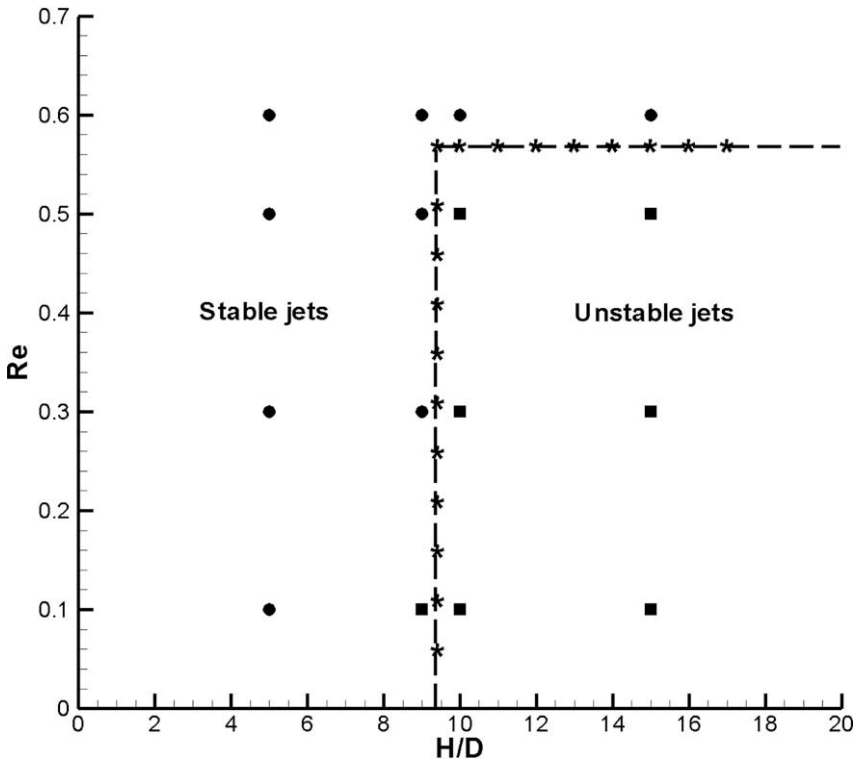

Fig. 27. Stability diagram for the injection of a viscous fluid in a cavity – comparison to experimental and analytical reference values – black circles correspond to stable jets, black squares to unstable jets and stars to the reference transition stability curve.

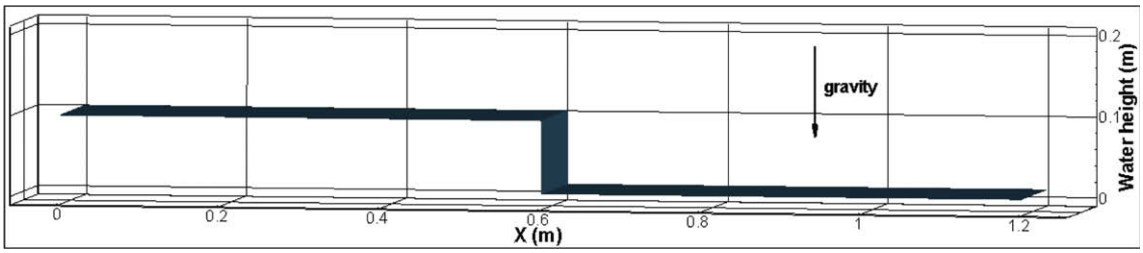

Fig. 28. Definition sketch of the three-dimensional dam-break flow of [45] – 600 × 20 × 100 grid.

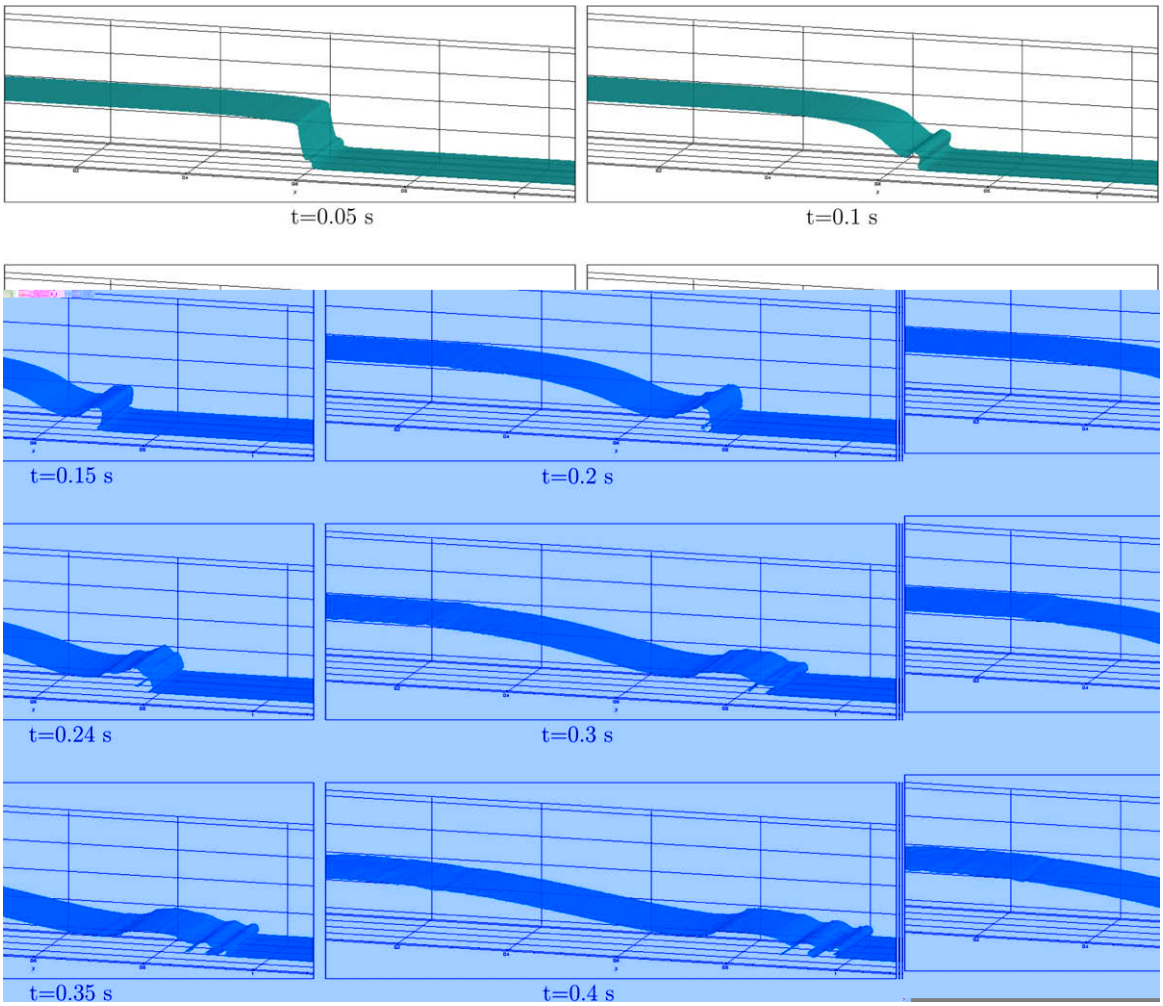

Fig. 29. Three-dimensional dam-break flow – isosurface $C = 0.5$. 600 × 20 × 100 grid and 27 ppc.

According to the theoretical and experimental investigations of [10], the buckling of a two-dimensional newtonian jet occurs when the following conditions are satisfied:

$$Re < 0.56 \quad \text{and} \quad H/D > 3\pi \tag{25}$$

where $Re = \frac{\rho_1 DU}{\mu_1}$, $H = 1$ m is the height of the square cavity and D is the diameter of the injector. Under these conditions, the jet alternatively travels through the computational domain from the left to the right, producing a so-called buckling phenomenon. The piling up of the liquid obstructs the oncoming flow that is consequently deviated. This results in a succession of layers between which air pockets can be trapped.

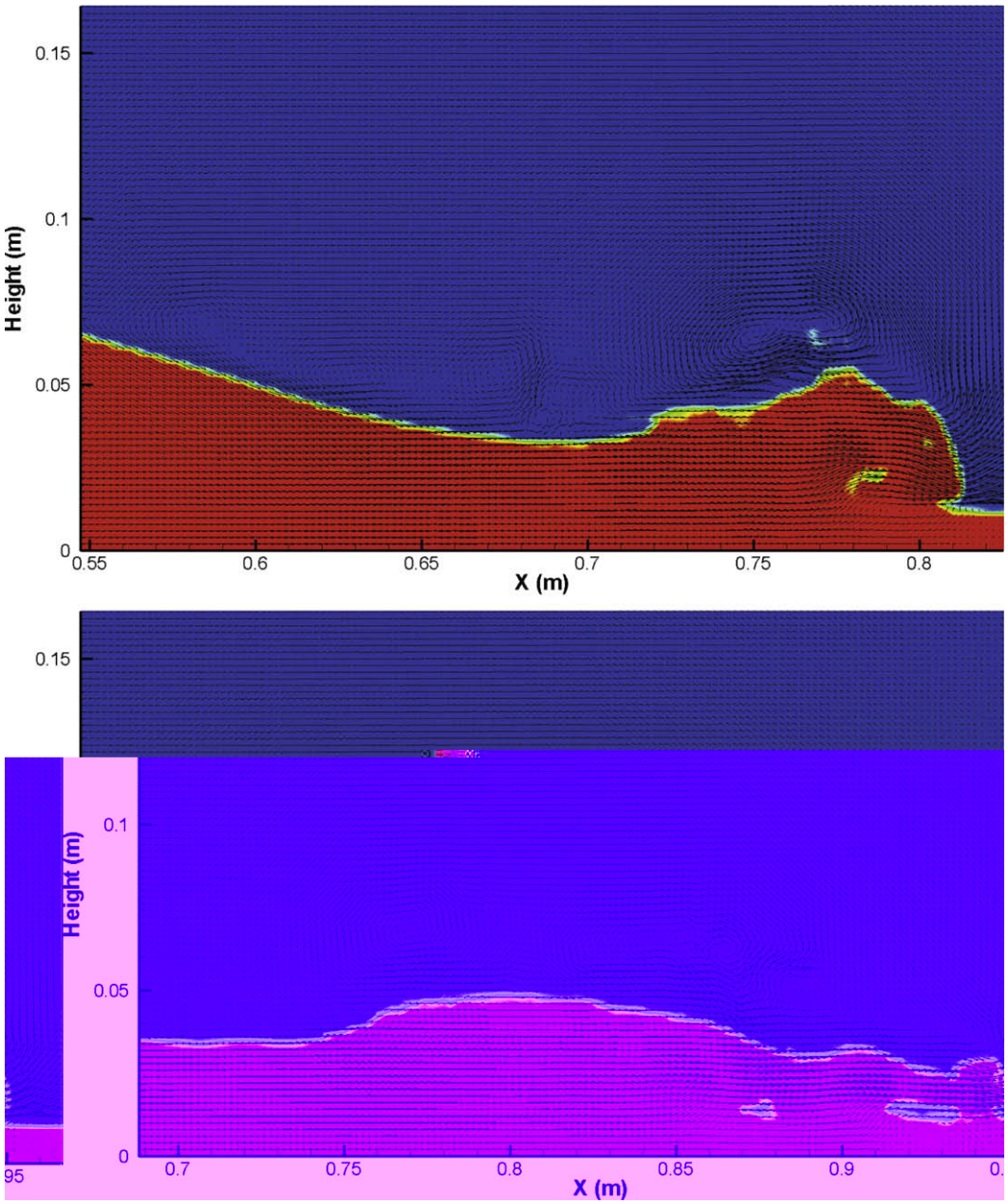

Fig. 30. Three-dimensional dam-break flow – Volume Of Fluid function $C = 1$ in red and $C = 0$ in blue) and velocity field in an X–Y slice are presented for $t = 0.24$ s and $t = 0.35$ s – $600 \times 20 \times 100$ grid and 27 ppc . (For interpretation of the references to color in this figure legend, the reader is referred to the web version of this article.)

The results of the simulation for several Re and H/D values are displayed in Fig. 26. The cavity filling under a viscous liquid jet injection is homogenous or undergoes buckling as predicted by theory [10]. As demonstrated in Fig. 26, trapped air parcels are captured by the method for $Re = 0.3$ and $H/D = 15$ or $Re = 0.1$ and $H/D = 9$, as a result of its non-diffusive behavior. The size of the air droplets is in this case determined by the size of the grid cell.

The above-mentioned test case illustrates the ability of the method to account for injection issues, through the redistribution of out-coming particles in the domain. Indeed, particles are expelled outside the domain, at the upper limit, by the outgoing velocity field. As described in Section 2.2.4, these particles are redistributed in rarefied cells, especially in cells corresponding to the injection area. Thus, the injection area is continuously seeded with new particles.

A stability diagram is presented in Fig. 27. The theoretical and experimental characteristic values of Re and H/D leading to instability are reported in this figure. Sixteen simulations have been carried out in order to characterize the numerical behavior of the jet in terms of buckling. A very good agreement was found between the reference values of [10] and the VOF-SM

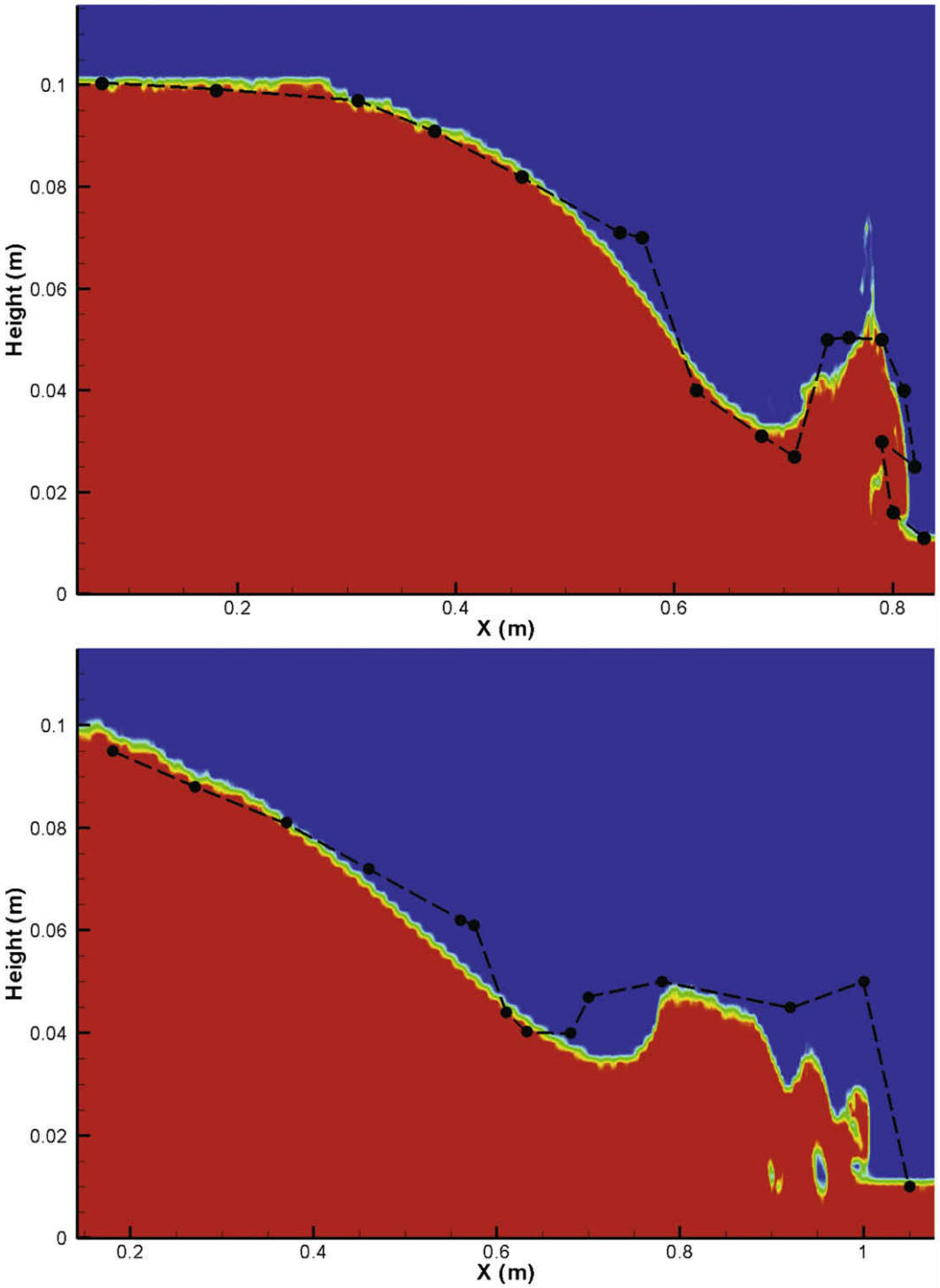

Fig. 31. Three-dimensional dam-break flow – Volume Of Fluid function $C = 1$ in red and $C = 0$ in blue) and experimental measurements of [45] (blackpoints) in an X–Y slice are presented for $t = 0.24$ s and $t = 0.4$ s – $600 \times 20 \times 100$ grid and 27 ppc . (For interpretation of the references to color in this figure legend, the reader is referred to the web version of this article.)

simulations. It can be observed that the case $Re = 0.1$ and $H/D = 9$ is the only case that does not follow the buckling conditions. This is probably due to the two-dimensional character of the simulations, to the axisymmetrical assumption of the analytical law (25) and the uncertainty of the measurements used by [10]. This case validates the accuracy and efficiency

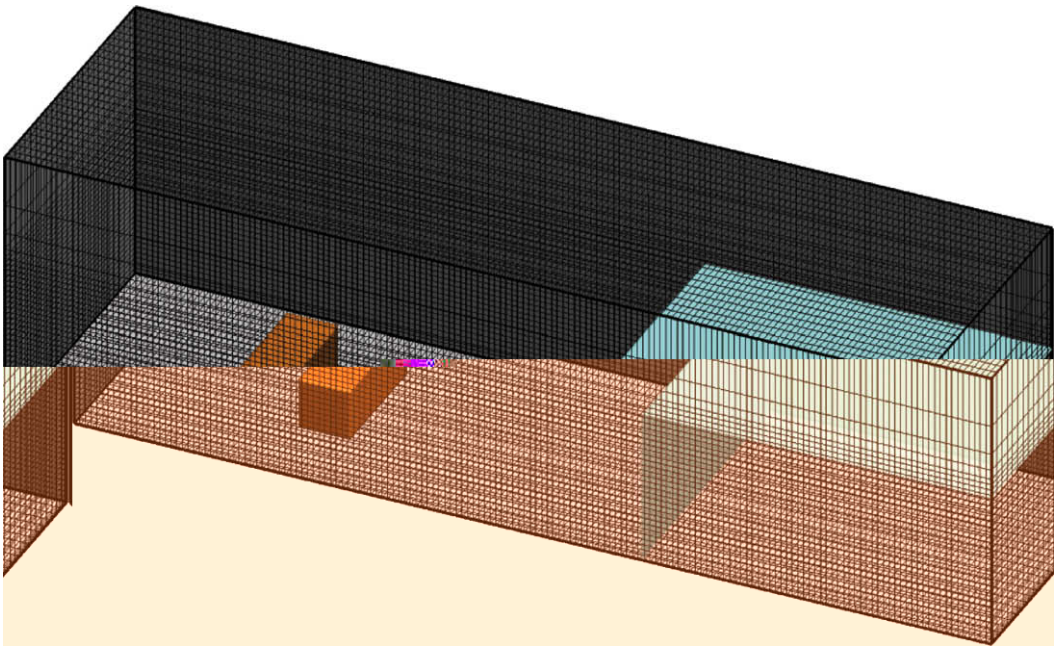

Fig. 32. Initial condition for the three-dimensional dam-break flow over an obstacle – Volume Of Fluid function ($C = 0.5$ in blue), obstacle in orange and computational grid for the coarser $161 \times 25 \times 35$ grid – 27 ppc are used. (For interpretation of the references to color in this figure legend, the reader is referred to the web version of this article.)

of the method for solving laminar two-phase flows involving unsteady behavior of free surfaces with connections between interfaces.

5.4. Three-dimensional dam-break flow

The three-dimensional dam-break flow resulting from the release of a water reserve on a still water level laying in front of the dam was considered. The dimensions and characteristics of the problem were chosen according to the case b in Fig. 3 of [45]. This configuration is interesting as the dam-break involves the generation of a forward jet that breaks in front of the initial dam. The unsteady behavior of the free-surface flow is characterized by interface ruptures and coalescence. In addition, measurements of the free surface, with a vertical plane light sheet, are available to validate the simulation results [45]. The initial condition is presented in Fig. 28: a still water reserve that is 0.1 m high and 0.6 m long upstream and 0.01 m high and 0.6 m long downstream is considered. The dam is located at $x = 0.6$ m. The flow channel is 0.4 m wide, and the numerical parameters are ppc $= 27$ and $\Delta t = 0.0001$ s, and the regular Cartesian grid is $600 \times 20 \times 100$.

The free-surface evolutions obtained with the VOF-SM simulations are presented in Fig. 29. The initial stages of the dam-break flow at $t = 0.05$ s and 0.1 s show the apparition of a forward jet that breaks downstream of the dam at $t = 0.24$ s and generates secondary jets and breaking processes from $t = 0.3$ s to $t = 0.4$ s. From a qualitative point of view, the free-surface flow is in good agreement with the non-linear potential flow computations and experiments of [45]. Fig. 30 proposes a zoom on the breaking zone at $t = 0.24$ s and $t = 0.35$ s. The velocity field is regular and continuous through the free surface, even if the right end of the breaking zone, in terms of wave behavior and Shallow-Water analysis [51], corresponds to a shock propagating from left to right. In addition, it can be observed that the VOF-SM approach remains compact and almost discontinuous at the interface, similarly to the most efficient VOF methods of the literature.

To finish, the VOF-SM simulations at $t = 0.24$ s and $t = 0.4$ s (see Fig. 31) in a median slice perpendicular to the initial dam are compared to the experiments of [45]. At $t = 0.24$ s, a very good agreement is found between both results in the rarefaction wave zone (left part of the dam-break flow) as well as in the shock zone (right part of the dam-break flow). Some irregularities are observed in the measurements, due to the difficult interpretation of the image in the free-surface zone where large amounts of foam exist. At $t = 0.4$ s, the simulations and experiments are also comparable, with many more differences in the shock zone. The velocity and height of the shock are very well predicted at these two reference times.

5.5. Three-dimensional dam-break flow over an obstacle

The three-dimensional dam-break flow over an obstacle corresponding to the experiments of [24] is now considered in order to evaluate the ability of the VOF-SM to handle real three-dimension free-surface flows. The fluids are water and air

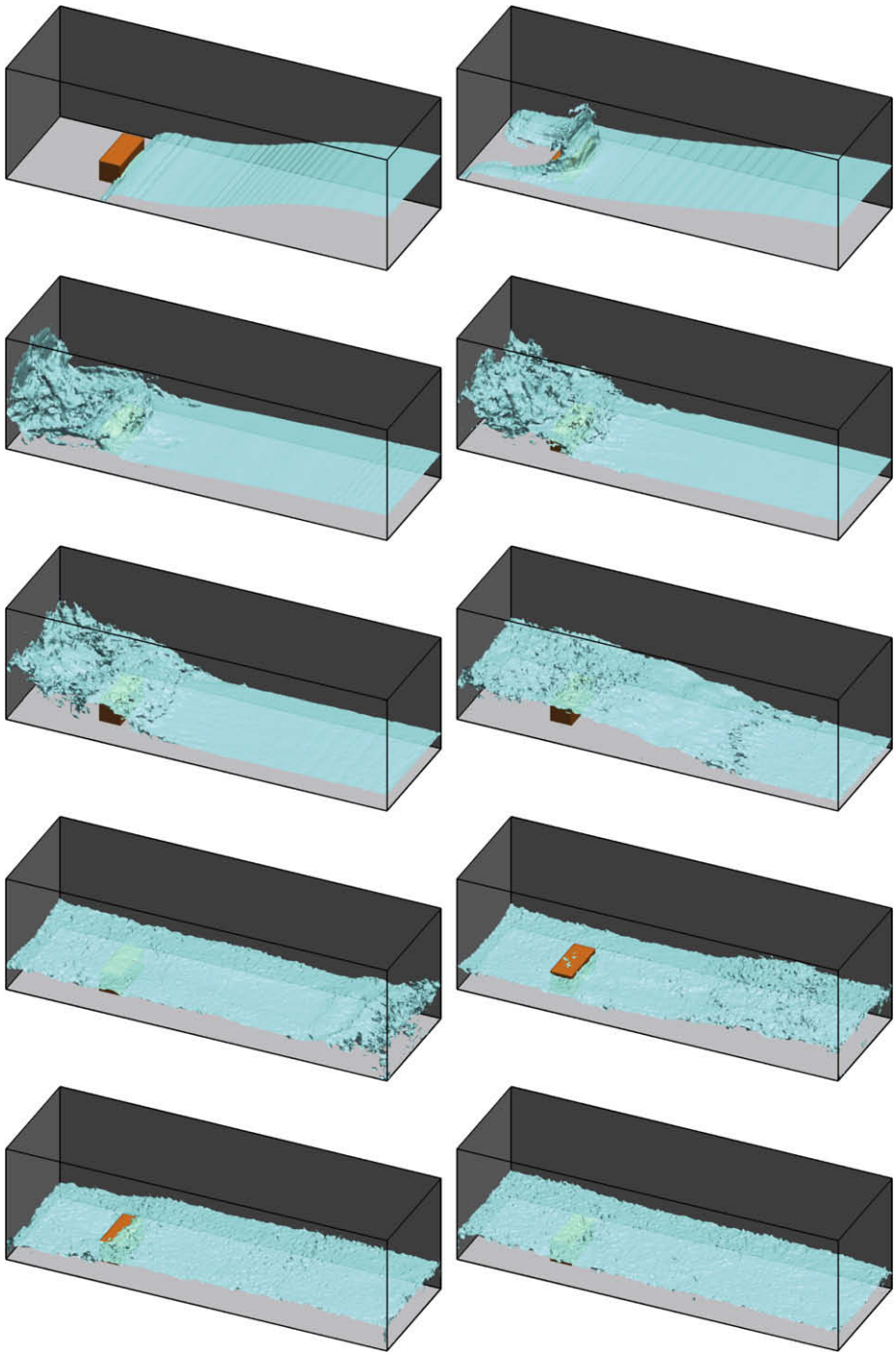

Fig. 33. Three-dimensional dam-break flow over an obstacle – Volume Of Fluid function $C = 0.5$ in blue and obstacle in orange – $161 \times 50 \times 35$ grid – 27 ppc are used – rom left to right and top to bottom, $t^* = 2.11, 3.17, 5.28, 6.33, 7.39, 10.56, 14.78, 17.95, 22.17$ and 29.56. (For interpretation of the references to color in this figure legend, the reader is referred to the web version of this article.)

and the dimensions of tank are 3.22 m × 1 m × 1 m. The initial water reserve dimensions are 1.228 m × 1 m × 0.55 m. Its initial height is noted h_0. The same probes H2, H4, P1, P3 and P5 as in [24] are used for the measurements of the pressure and vertical free-surface elevation to be compared with the experiments of [24]. The initial condition is presented in Fig. 32. Two computational grids are considered for grid convergence, containing $161 \times 25 \times 35$ (140,875 elements) and $161 \times 50 \times 35$ (281,750 elements) grid cells. The grid is constant along the X- and Y- axis while a constant space step is chosen along the Z-axis for $0 < z < 0.6$ (30 cells) with an exponential grid zone for $0.6 < z < 1$ (5 cells). The different stages of

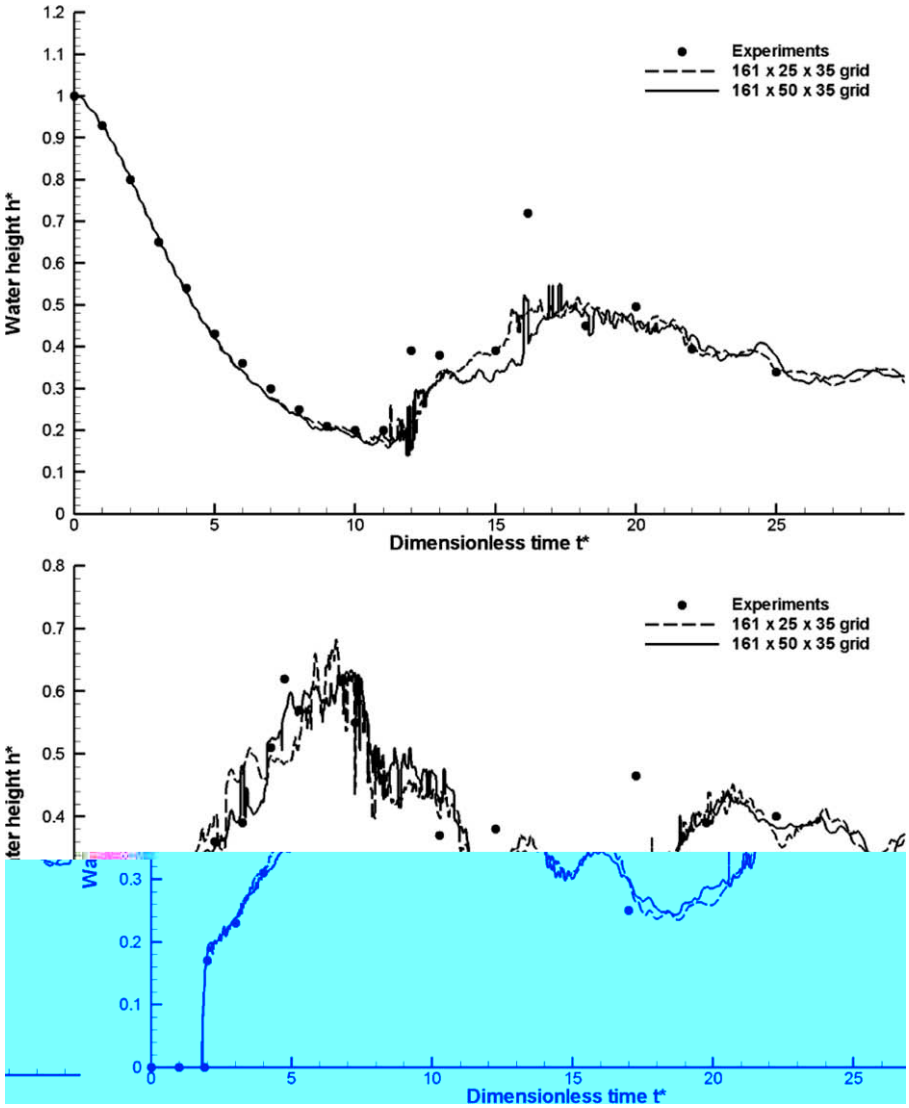

Fig. 34. Time evolution of dimensionless vertical water heights h^* according to dimensionless time h^* for probe H4 (top) and H2 (bottom).

the dam-break flow over the parallelepiped obstacle is illustrated in Fig. 33. The obstacle is numerically modeled thanks to a fictitious domain approach and a penalty method according to the works of [23,53]. The results are in good agreement with previous numerical simulations realized by [24,39]. It can be noted that the Lagrangian management of the VOF function C induces a less regular behavior of the $C = 0.5$ isoline, i.e. the free surface. In addition, more bubbles and small interfacial structures are observed when the dam-break wave interacts with the obstacles and the walls of the tank. In the two cases, thanks to the good conservation of the mass advected by the Lagrangian markers, the maximum relative mass error estimated as the integral of the Eulerian VOF function C is between 1% and 2%.

Concerning the computational time involved by the VOF-SM, a comparison has been realized on the two grids between the VOF-SM and the VOF-PLIC method of [56]. These values have been compared to the time required to solve the Navier–Stokes equations with the augmented Lagrangian method when 60 iterations are considered in the iterative solver. These values involve a time almost equivalent to the time required by a time splitting method for solving the mass and momentum equations. On a 2.2 GHz Intel Centrino processor with 2 Mo central memory, the VOF-SM, VOF-PLIC and Navier–Stokes solving requires respectively in average 8.5, 0.06 and 26 s on the coarser grid and 16.8, 0.13 and 61 s on the finer mesh. It appears clearly that the VOF-SM is expansive compared to a standard interface tracking method. However, even in its globally seeded version (more than 3.8 and 7.6 millions of particles are managed on the two grids), the time dedicated to the VOF-SM remains three times lower than the time required by the Navier–Stokes solver. The VOF-SM time cost could be drastically reduced by seeding locally the Lagrangian markers in the vicinity of the interface. This local Lagrangian mesh refinement version of VOF-SM is under development and will be presented in the near future.

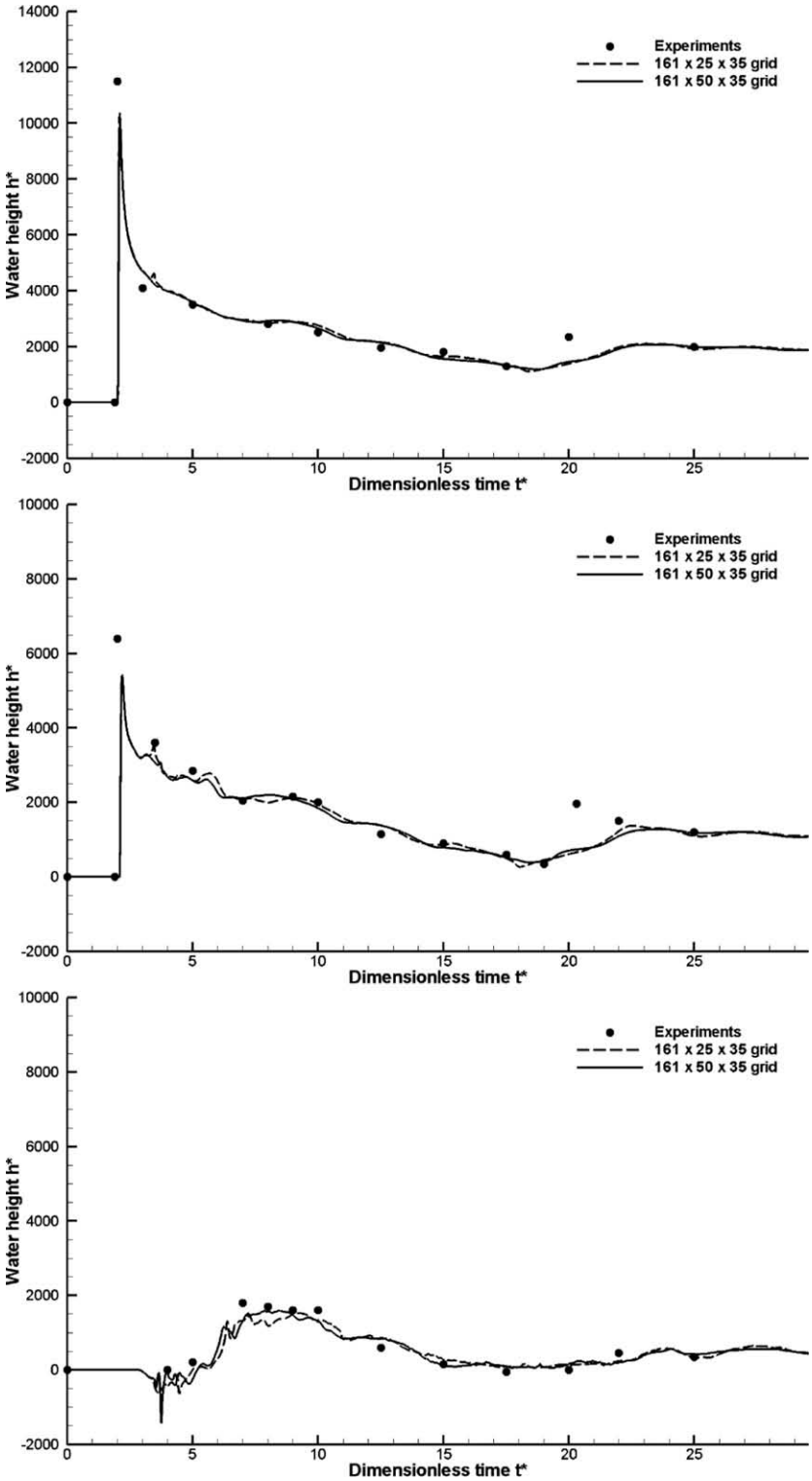

Fig. 35. Time evolution of pressure according to dimensionless time t^* for probe P1 (top), P3 (middle) and P5 (bottom).

The quantitative validation of the numerical simulations can be achieved thanks to the comparison of the vertical free surface and pressure measurements at probe H2, H4, P1, P3 and P5. Dimensionless time t^* and vertical water height h^* are introduced such that $t^* = t\sqrt{(g/h_0)}$ and $h^* = h/h_0$. In Fig. 34 are presented the comparison of the numerically and experimentally obtained vertical water heights according to time. A global very good agreement is found between measurements

and simulations. The major discrepancies are observed for $t^* = 16$ concerning probe H4 and for $t^* = 20$ concerning probe H2, as in the simulations of [39]. No major differences are observed between the two grids, demonstrating the macroscopic convergence of the simulations. The pressure values of probe P1, P3 and P5 on the obstacle are presented in Fig. 35. As for the vertical free-surface elevation, the numerical pressure probes provides values very close to the experimental ones. The only important difference is observed for the three curves for $t^* = 20$. The same gap is described in the work of [39], perhaps corresponding to a bad value concerning the positioning of the probes along the Y-axis. This validation problem confirms the potential of the VOF-SM to deal accurately with free-surface flows on irregular grids, even with less than 200000 elements in three dimensions.

6. Conclusions and perspectives

A new Volume Of Fluid Sub-Mesh (VOF-SM) method for the simulation of scalar interface advection or transport issues was presented. The method is based on a Eulerian representation of the VOF or concentration functions thanks to a Lagrangian sub-mesh description that employs Lagrangian markers to build a local Eulerian concentration. The VOF-SM method is able to simulate interface tracking as well as concentration transport problems on orthogonal curvilinear grids in three dimensions.

It could be demonstrated that the VOF-SM method is at least of second order regardless of the grid irregularity or the complexity of the initial VOF or concentration profile. The results provided by the VOF-SM approach are one to two orders of magnitude better than the best VOF or advection schemes found in the literature. Concerning incompressible free-surface flow simulations, the VOF-SM method, coupled to an augmented Lagrangian method, was validated in two dimensions on the filling of a square cavity by a viscous fluid. The stability diagram of [10] concerning buckling jets could be nicely recovered and validated the ability of the VOF-SM method to simulate free-surface flows. The VOF-SM method was also evaluated on the three-dimensional dam-break flow over a wet bottom. The behavior of the simulations were in good agreement with the experiments and computations of [45]. The quantitative and unsteady behavior of the VOF-SM approach was validated in this case.

On a physical point of view, the numerical modeling of surface tension forces is not presented in this article as it requires a special attention. The Continuum Surface Force (CSF) of [6] has been used with the VOF-SM by using the Eulerian VOF function C to estimate a volume force added in the momentum equation, as is classically done in VOF or level-set methods. It can be imagined to benefit from the Lagrangian description of the two-phase flow so as to estimate the capillary effects by using the concentration advected by the Markers as in SPH methods. Specific developments are under progress concerning the surface tension forces with the VOF-SM approach which will be presented in future articles.

Future developments of the VOF-SM approach will be devoted to improving the local particle distribution near the interface so as to optimize the computation time. In addition, the particle remeshing will have to be improved, for example by using Kernel functions as proposed in [3,9,25,7]. Moreover, in the Lagrangian advection step of the markers, a correction of the particle velocity [7] will be evaluated in order to ensure mass conservation at the Lagrangian scale. To finish, parallel implementations of the VOF-SM method will have to be considered. It seems natural to implement this point with distribute memory supercomputers as the VOF-SM algorithm only requires local information in order to build the Eulerian VOF or concentration profiles. The major difficulty lies in the exchange of the markers between the sub-domains attached to the processors.

The VOF-SM method is a numerical tool that provides a description of the multiphase flow at a scale smaller than the Eulerian grid cell. It is a first step in carrying out sub-mesh physical modeling of multiphase flows involving LES turbulence models [30,26,54] or small-scale interfacial structures with specific drag forces, coalescence or rupture processes. Applications to fuel injection in engines, interaction between plasma and liquid jets or wave breaking [31,34] are affected by these models.

Acknowledgments

We acknowledge the reviewers for their fruitful remarks and helpful suggestions that guide us in improving this article. The authors also thank the French Commissariat a l'Energie Atomique (CEA) for its financial support.

References

[1] E. Aulisa, S. Manservisi, R. Scardovelli, S. Zaleski, A geometrical area-preserving volume-of-fluid advection method, J. Comput. Phys. 192 (2003) 355–364.
[2] E. Aulisa, S. Manservisi, R. Scardovelli, S. Zaleski, Interface reconstruction with least-squares fit and split advection in three-dimensional Cartesian geometry, J. Comput. Phys. 225 (2007) 2301–2319.
[3] J.T. Beale, On the accuracy of vortex methods at large times, in: B. Engquist, M. Luskin, A. Majda (Eds.), Computational Fluid Dynamics and Reacting Gas Flows, Springer-Verlag, New York, 1988.
[4] F. Bierbrauer, S.P. Zhu, A numerical model for multiphase flow based on the GMPPS formulation. Part I: Kinematics, Comput. Fluids 36 (2007) 1199–1212.
[5] A. Bott, A positive definite advection scheme obtained by nonlinear renormalization of the advective flux, Mon. Wea. Rev. 117 (1989) 1006–1015.
[6] J.U. Brackbill, D.B. Kothe, C. Zemach, A continuum method for modeling surface tension, J. Comput. Phys. 100 (1992) 335–354.

[7] A.K. Chaniotis, D. Poulikakos, P. Koumoutsakos, Remeshed smoothed particle hydrodynamics for the simulation of viscous and heat conducting flows, J. Comput. Phys. 182 (2002) 67–90.
[8] G.-H. Cottet, P. Poncet, Advances in direct numerical simulations of 3D wall-bounded flows by vortex-in-cell methods, J. Comput. Phys. 193 (2003) 136–158.
[9] G.H. Cottet, Artificial viscosity models for vortex and particle methods, J. Comput. Phys. 127 (1996) 299–308.
[10] J.O. Cruickshank, Low Reynolds number instabilities in stagnating flows, J. Fluid Mech. 193 (1988) 111–127.
[11] S. Dhaniyala, A.S. Wexler, Numerical schemes to model condensation and evaporation of aerosols, Atmos. Env. 30 (1996) 919–928.
[12] V. Daru, C. Tenaud, High order one-step monotonicity-preserving schemes for unsteady compressible flow calculations, J. Comput. Phys. 193 (2004) 563–594.
[13] D. Enright, R. Fedkiw, J. Ferziger, I. Mitchell, A hybrid particle level set method for improved interface capturing, J. Comput. Phys. 183 (2002) 83–116.
[14] R. Fedkiw, S. Osher, Level set methods: an overview and some recent results, J. Comput. Phys. 169 (2001) 463–502.
[15] M. Fortin, R. Glowinski, Methodes de Lagrangien augmente, Application a la resolution numerique de problemes aux limites, Paris, Dunod, 1982.
[16] H. Friess, D. Lakehal, S. Vincent, Interface tracking based on an imposed velocity field in a convergent–divergent channel (PN), Multiphase Sci. Tech. 16 (2004) 163–168.
[17] J.R. Chawner, J.P. Steinbrenner, N. Wyman, Hybrid grid generation for complex geometries using Gridgen, in: Seventh International Grid Conference, Whistler, British Columbia, Canada, June 25, 2000.
[18] I. Gustafsson, On first and second order symmetric factorization methods for the solution of elliptic difference equations, Chalmers University of Technology, 1978.
[19] C.W. Hirt, B.D. Nichols, Volume of fluid (VOF) method for the dynamics of free boundaries, J. Comput. Phys. 39 (1981) 201–225.
[20] M.E. Hubbard, A.L. Laird, Achieving high-order fluctuation splitting schemes by extending the stencil, Comput. Fluids 34 (2005) 443–459.
[21] E. Ishii, T. Ishikawa, Y. Tanabe, Hybrid particle/grid method for predicting motion of micro- and macro-free surfaces, J. Fluid Eng. 128 (2006) 921–930.
[22] G.S. Jiang, C.W. Shu, Efficient implementation of weighted essentially non-oscillatory schemes, J. Comput. Phys. 126 (1996) 202–228.
[23] K. Khadra, P. Angot, S. Parneix, J.P. Caltagirone, Fictitious domain approach for numerical modelling of Navier–Stokes equations, Int. J. Numer. Meth. Fluids 34 (2000) 651–684.
[24] K.M.T. Kleefsman, G. Fekken, A.E.P. Veldman, B. Iwanowski, B. Buchner, A volume-of-fluid based simulation method for wave impact problems, J. Comput. Phys. 206 (2005) 363–393.
[25] P. Koumoutsakos, Inviscid axisymmetrization of an elliptical vortex, J. Comput. Phys. 138 (1997) 821–857.
[26] E. Labourasse, D. Lacanette, A. Toutant, P. Lubin, S. Vincent, O. Lebaigue, J.-P. Caltagirone, P. Sagaut, Towards large eddy simulation of isothermal two-phase flows: governing equations and a priori tests, Int. J. Multiphase Flow 33 (2007) 1–39.
[27] D. Lacanette, A. Gosset, S. Vincent, J.-M. Buchlin, E. Arquis, Macroscopic analysis of gas-jet wiping: numerical simulation and experimental approach, Phys. Fluids 18 (2006) 1–15.
[28] R.J. LeVeque, Numerical methods for conservation laws, in: Lecture in Mathematics, Birhauser, Zurich, 1990.
[29] Q. Li, S. Fu, K. Xu, A compressible Navier–Stokes flow solver with scalar transport, J. Comput. Phys. 204 (2005) 692–714.
[30] P. Liovic, D. Lakehal, Interface–turbulence interactions in large-scale bubbling processes, Int. J. Heat Fluid Flow 28 (2007) 127–144.
[31] P. Liovic, D. Lakehal, Multi-physics treatment in the vicinity of arbitrarily deformable gasliquid interfaces, J. Comput. Phys. 222 (2007) 504–535.
[32] J. Liu, S. Koshisuka, Y. Oka, A hybrid particle-mesh method for viscous, incompressible, multiphase flows, J. Comput. Phys. 202 (2005) 65–93.
[33] J. Lopez, J. Hernandez, P. Gomez, F. Faura, An improved PLIC-VOF method for tracking thin fluid structures in incompressible two-phase flows, J. Comput. Phys 208 (2005) 51–74.
[34] P. Lubin, S. Vincent, S. Abadie, J.-P. Caltagirone, Three-dimensional large eddy simulation of air entrainment under plunging breaking waves, Coastal Eng. 53 (2006) 631–655.
[35] J.C. Martin, W.J. Moyce, An experimental study of the collapse of liquid columns on a rigid horizontal plane, Phil. Trans. Royal Soc. London 244 (1952) 312–324.
[36] K. Nguyen, D. Dabdub, Two-level time marching scheme using splines for solving the advection equation, Atmos. Env. 35 (2001) 1627–1637.
[37] K. Nguyen, D. Dabdub, Development and analysis of a non-splitting solution for three-dimensional air quality models, Atmos. Env. 37 (2003) 3741–3748.
[38] A. Oliveira, A.B. Fortunato, Toward an oscillation-free, mass conservative, Eulerian–Lagrangian transport model, J. Comput. Phys. 183 (2002) 142–164.
[39] I.R. Park, K.S. Kim, J. Kim, S.H. Van, A volume-of-fluid method for incompressible free surface flows, Int. J. Numer. Meth. Fluids, doi: 10.1002/fld.2000, 2009.
[40] S.V. Patankar, Numerical Heat Transfer and Fluid Flow, Hemisphere Publishing Corporation, New York, 1980.
[41] P. Raad, R. Bidoae, Three-dimensional Eulerian–Lagrangian marker and micro cell method for the simulation of free surface flows, J. Comput. Phys. 203 (2005) 668–699.
[42] W. Rider, D. Kothe, Reconstructing volume tracking, J. Comput. Phys. 141 (1998) 112–152.
[43] R. Scardovelli, S. Zaleski, Direct numerical simulation of free surface and interfacial flows, Ann. Rev. Fluid. Mech. 31 (1999) 567–603.
[44] O. Schenk, K. Gartner, W. Fichtner, A. Stricker, PARDISO: a high-performance serial and parallel sparse linear solver in semiconductor device simulation, J. Future Gener. Comput. Sys. 18 (2001) 69–78.
[45] P.K. Stansby, A. Chegini, T.C.D. Barnes, The initial stages of dam-break flow, J. Fluid Mech. 374 (1998) 407–424.
[46] V.A. Titarev, E.F. Toro, WENO schemes based on upwind and centred TVD fluxes, J. Comput. Phys. 34 (2005) 705–720.
[47] G. Tryggvason, B. Bunner, A. Esmaeeli, D. Juric, N. Al-Rawahi, W. Tauber, J. Han, S. Nas, Y.-J. Jan, A front tracking method for the computations of multiphase flows, J. Comput. Phys. 169 (2001) 708–759.
[48] H.A. Van Der Vorst, Bi-CGSTAB: a fast and smoothly converging variant of Bi-CG for the solution of nonsymmetric linear systems, SIAM J. Sci. Stat. Comput. 13 (1992) 631–644.
[49] S. Vincent, J.-P. Caltagirone, Efficient solving method for unsteady incompressible interfacial flow problems, Int. J. Numer. Meth. Fluids 30 (1999) 795–811.
[50] S. Vincent, J.-P. Caltagirone, A one-cell local multigrid method for solving unsteady incompressible multiphase flows, J. Comput. Phys. 163 (2000) 172–215.
[51] S. Vincent, P. Bonneton, J.-P. Caltagirone, Numerical modelling of bore propagation and run-up on sloping beaches using a Mac-Cormack TVD scheme, J. Hydraul. Res. 39 (2001) 41–49.
[52] S. Vincent, J.-P. Caltagirone, P. Lubin, T.N. Randrianarivelo, An adaptative augmented Lagrangian method for three-dimensional multimaterial flows, Comput. Fluids 33 (2004) 1273–1299.
[53] S. Vincent, T.N. Randrianarivelo, G. Pianet, J.-P. Caltagirone, Local penalty methods for flows interacting with moving solids at high Reynolds numbers, Comput. Fluids 36 (2007) 902–913.
[54] S. Vincent, J. Larocque, D. Lacanette, A. Toutant, P. Lubin, P. Sagaut, Numerical simulation of phase separation and a priori 3 two-phase LES filtering, Comput. Fluids 37 (2008) 898–906.
[55] F. Xiao, X. Peng, A convexity preserving scheme for conservative advection transport, J. Comput. Phys. 198 (2004) 389–402.
[56] D.L. Youngs, K.W. Morton, M.J. Baines, Time-dependent multi-material flow with large fluid distortion, in: Numerical Methods for Fluid Dynamics, Academic Press, New York, 1982.